2022-12-01

Magnetic Structures of Sawtooth Olivines Mn2SiX 4 (X = S, Se) Determined Through Neutron Powder Diffraction

Melaku Sisay Tafere
University of Texas at El Paso

MAGNETIC STRUCTURES OF SAWTOOTH OLIVINES Mn_2SiX_4 (X = S, Se) DETERMINED THROUGH NEUTRON POWDER DIFFRACTION

MELAKU S. TAFERE

Master's Program in Physics

APPROVED:

Harikrishnan Nair, Ph.D., Chair

Rajendra Zope, Ph.D.

Zhang, Qiang, Ph.D.

Stephen Crites, PhD.

Dean of the Graduate School

Dedicated

to my families

and friends

MAGNETIC STRUCTURES OF SAWTOOTH OLIVINES Mn_2SiX_4 (X = S, Se) DETERMINED THROUGH NEUTRON POWDER DIFFRACTION

by

MELAKU S. TAFERE

THESIS

Presented to the Faculty of the Graduate School of

The University of Texas at El Paso

in Partial Fulfillment

of the Requirements

for the Degree of

MASTER OF SCIENCE

Department of Physics

THE UNIVERSITY OF TEXAS AT EL PASO

December 2022

Acknowledgements

First of all, I would like to thank God for everything. I would like to express my deepest gratitude to my supervisor, Dr. Harikrishnan Nair, for the support and guidance throughout the research.

I would like to express my appreciation to Dr Mark Pederson for welcoming me and for the induction about UTEP environment and for his instant response to all my queries from course work to the end of my stay.

Thank you to the UTEP physics department students and staff. My roommate Dr Ramon Sanchez and all your family are always amazing, can't wait to visit DR.

I would like to thank Dr. Wossen Belachew and Mulu Birhan for all your help in everything and for showing love and courage.

I am also very thankful to all Elpaso international community for all your support and love.

Finally, I would like to acknowledge the Ethiopian community(my family) in El paso, you guys are amazing.

Abstract

In olivine chalcogenide Mn_2SiX_4 (X = S, Se) compounds, the Mn lattice produces a sawtooth, which is of critical significance in magnetism due to the potential for manifesting at bands in the magnon spectrum, a crucial component in magnonics. The compounds Mn_2SiS_4 and Mn_2SiSe_4 in Mn_2SiX_4 family undergo antiferromagnetic phase transitions at T $\approx$ 85 K and $\approx$ 66 K, respectively, as determined from the specific heat, C_p(T). The average and local crystal structures are determined using synchrotron X-ray, neutron diffraction, and X-ray total scattering data followed by Rietveld and pair distribution function (PDF) analysis. It is found from PDF that the Mn triangle that constitutes the sawtooth is isosceles in Mn_2SiS_4 whereas it is nearly equilateral in Mn_2SiSe_4. The magnetic phase transitions in Mn_2SiX_4 seen in bulk measurements are confirmed using neutron diffraction in this work, and the magnetic structures accurately estimated. We find that the Mn spins adopt a ferromagnetic alignment on the sawtooths in both Mn_2SiS_4 and Mn_2SiSe_4 but along different crystallographic directions. By following the thermal evolution of the refined magnetic moment at the Mn site, obtained from refining the neutron diffraction data, the transition temperatures are accurately determined as T_N(S) = 83(2) K and T_N(Se) = 70.0(5) K. The magnetic space groups are determined as $Pnma$ and $Pnm'a'$ for Mn_2SiS_4 and Mn_2SiSe_4, respectively. The magnetic excitations studied using inelastic neutron scattering reveal a magnon excitation with an energy corresponding to 4.5 meV in both the compounds.

Melaku S. Tafere

Table of Contents

Page

List of Figures

List of Tables

Chapter 1

Olivines

The chemical formula for olivine is B_2AX_4 (orthorhombic space group $Pnma$), and its X anions have almost regular hexagonal close-packed (hcp) dispositions, while the A cations are in tetrahedral coordination and the B cations are in distorted octahedral coordinations[1]. There are four magnetic ions per cell on $4a$ sites with inversion symmetry and four magnetic ions per cell on $4c$ sites with mirror symmetry in the case of the magnetic olivines (B = Mn, Fe, Co). The $4a$ positions coordinates are as follows: (0, 0, 0); (0, $\frac{1}{2}$, 0); ($\frac{1}{2}$, 0, $\frac{1}{2}$); ($\frac{1}{2}$, $\frac{1}{2}$, $\frac{1}{2}$), and the coordinates for the $4c$ atoms inside the cell are: (x, $\frac{1}{4}$, z); (-x, $\frac{3}{4}$, -z); ($\frac{1}{2}$-x, $\frac{3}{4}$, $\frac{1}{2}$+z); ($\frac{1}{2}$ + x, $\frac{1}{4}$, $\frac{1}{2}$ - z), where for each type of olivine, x and z must be determined by neutron or X-ray diffraction. The olivine structure is the hcp counterpart of the spinel structure and is exemplified by the minerals forsterite (Mg_2SiO_4) and triphylite ($LiFePO_4$)[2]. Within a hcp array of O atoms, Si or P occupy one-eighth of the tetrahedral sites, Mg or Li occupy half of the octahedral sites, and Fe occupy half of the octahedral sites. Li and Fe in $LiFePO_4$ occupy two crystallographically different octahedral positions in olivine, which are occupied in an orderly fashion. Figure 1.0.1 shows the crystal structure, while Table 1.1 lists various olivines. Olivines are mostly made up of oxides, but they can also contain sulfides, selenides, and fluorides. In oxides, the three cations have a net charge of 8^+ due to various cation charge combinations[2]. The major mineralogical constituents of the Earth's upper mantle are assumed to be olivines (mostly forsterite, Mg_2SiO_4) and fayalite, Fe_2SiO_4. Many olivines transform to spinel structure at high pressures, and spinels are most likely the major element of the Earth's lower mantle. The creation of mountain ranges and undersea ridges may have been influenced by the volume variations related with the olivine to spinel phase changeover throughout the Earth's evolution. Due to the drop in pressure, spinel material from the lower mantle was forced upwards to the Earth's surface and converted into

olivine.

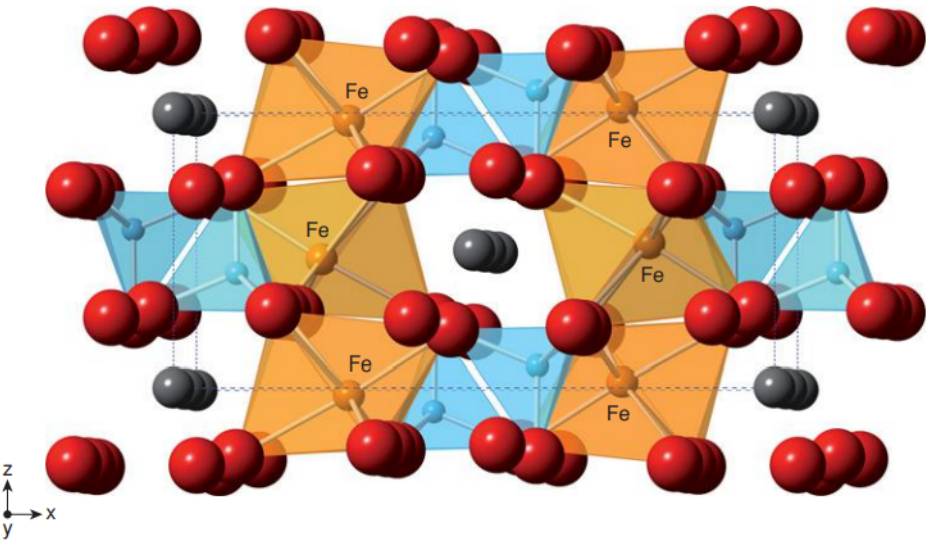

Figure 1.0.1: Olivine structure of $LiFePO_4$. The black sphere is Li, the cyan color is P and the red is O. Image taken from [2].

Table 1.1: Some compounds that crystallize in the olivine structure. The octahedral and tetrahedral sites are related to valency of cations (positively charged) and anions (negatively charged) and coordination number.

General formula			
Octahedral site	Tetrahedral site	hcp anion	Examples
II	IV	O_4	Mg_2SiO_4 (forsterite) Fe_2SiO_4 (fayalite) Ca,Mg SiO_4 (monticellite) γ -Ca2SiO_4 A_2GeO_4: A = Mg, Ca, Sr, Ba, Mn
III	II	O_4	Al_2BeO_4 (chrysoberyl) Cr_2BeO_4
II, III	III	O_4	$MgAlBeO_4$
I, II	V	O_4	$LiFePO_4$ (triphylite) $LiMnPO_4$ (lithiophylite)
I, III	IV	O_4	Li$RE$$SiO_4$: RE = Ho, . . . , Lu Na$RE$$GeO_4$: RE = Sm, . . . , Lu Li$RE$$GeO_4$: RE = Dy, . . . , Lu
II	IV	S_4	Mn_2SiS_4 Mg_2SnS_4 Ca_2GeS_4
I	II	F_4	γ-Na_2BeF_4

1.1 Physical properties of olivines

Despite the phase transition temperatures (T_N) noted in the magnetic susceptibility and the notable variation in the magnitude of magnetic susceptibility seen for the two sets of compositions in Figure 1.1.1 panels (a) and (b). In the instance of Mn_2SiS_4, the magnetic phase transition manifests as a sharp anomalous peak at $T_N = 83.7$ K. The peak at the phase transition weakens when S is gradually replaced by Se, and eventually, for Mn_2SiSe_4, a very broad feature is observed below ≈ 65 K[3].

A similar compound iron chalcogenides, particularly iron pyrite was investigated[4], which has promising future to be a useful material for cost effective thin film photovoltaics. Fe_2MS_4 (M = Ge, Si), a different class of iron chalcogenides that has been suggested as a potential replacement for pyrite, has only been studied for its remarkable magnetic properties. The compounds have the potential to be used in solar cells because they are p-type and easily create photo current[4]. Another motivation for the study of olivine chalcogenides is their high thermopower. Similar compounds Fe_2GeS_4 and Fe_2GeSe_4 were investigated for the thermoelectric properties and showed a high thermopower above 300 μV K^{-1}[5]. The report found that Fe_2GeTe_4 exhibits a bipolar thermoelectric nature as a result of its narrow band gap. Comparing the olivine type Fe_2GeCh_4 (Ch = S, Se and Te) structure to the marcasite and pyrite structures, it is discovered to have a greater estimated thermopower. Fe_2GeS_4 and Fe_2GeSe_4 among the studied systems have excellent thermoelectric characteristics, particularly along the b and c axes. Because of the band structure features in Mn_2SiS_4 and Mn_2SiSe_4) these materials could be useful for thermoelectric applications[3]. The study indicates both compounds exhibit thermal conductivity resembling that of semiconducting materials, where phonons predominate the heat transport. At low temperatures, the thermal conductivity rapidly rises with temperature, forming a noticeable maximum below 50 K, before dropping to room temperature. The maximum occurs at low temperatures because thermal scattering is lower there

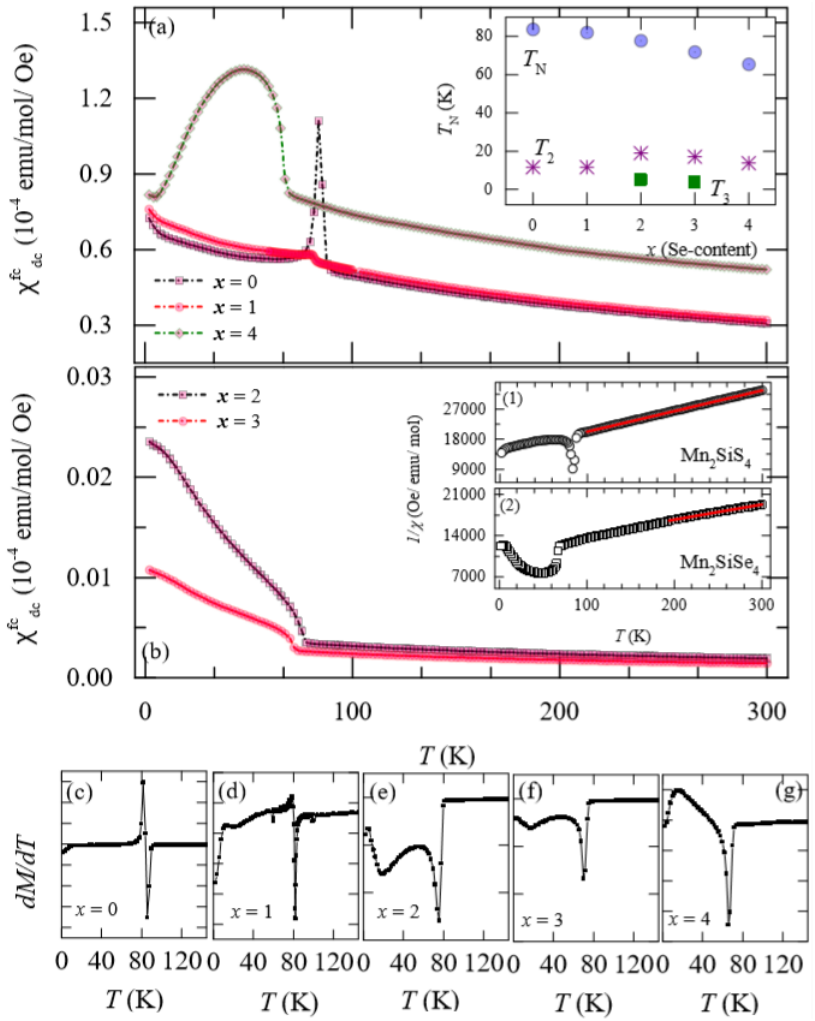

Figure 1.1.1: The magnetic susceptibility of $Mn_2SiS_{4-x}Se_x$ (x = 0-4) obtained in 500 Oe field cooled condition presented for the x = 0, 1, 4 in panel(a) and x = 2, 3 in panel(b). The inset of panel(a)shows the T_N's as a function of Se-content(x). The insets (1) and (2) in panel(b) shows the $1/\chi^{fc}_{dc}(T)$ curves of Mn_2SiS_4 and Mn_2SiSe_4 respectively along with Curie-Weiss fit(red solid line).(c-g)The derivative, dM/dT versus temperature showing the multiple anomalies present in each composition[3].

Fe_2GeSe_4 exhibits a similar trend for the indirect band gap[1] along the Γ of the valence band maximum (VBM) and at the e conduction band minimum (CBM). Nevertheless, it is discovered that Fe_2GeTe_4 is a direct band gap semiconductor[2], with both the VBM and CBM occurring at

[1]Indirect band gap semiconductor, the maximum energy of the valence band occurs at a different value of momentum to the minimum in the conduction band energy.

[2]Direct band gap semiconductor, the top of the valence band and the bottom of the conduction band occur at the same value of momentum.

Γ point. The hybridization[3] between Fe-Ch states is provided by the octahedra that are created when Fe and Ch combine. The Fe-3d orbitals are separated into three filled represented by t_{2g} and empty doublet represented by e_g states by the octahedral crystal field splitting. Figure 1.1.2 presents a schematic illustration of the crystal field splitting of Fe-3d. The full triplet states of t_{2g}, together with a negligibly small amount from Fe-3de_g and S-3p, contribute to the VBM as non-bonding states. The chalcogen-p states and the empty doublet states of Fe-3de_g combine to generate the bonding states below the VBM. The anti-bonding states that make up the CBM are formed by the higher energy states of chalcogen-p and Fe-3de_g. In suitably ordered systems,

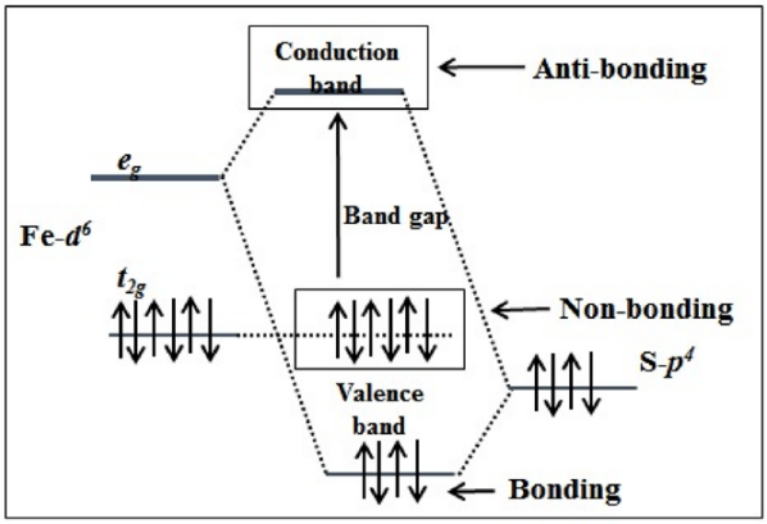

Figure 1.1.2: Schematic representation of octahedral crystal field splitting of Fe-d states in Fe_2GeCh_4 [5].

certain magnetic structural motifs, such as corner-sharing triangles of isotropic transition-metal ions, can lead to geometric frustration if the interaction between spins is antiferromagnetic. The Mn lattice's sawtooth-like triangular arrangement is the key structural characteristic of Mn_2SiX_4 compounds from the perspective of magnetism [6]. Magnetic compounds with a saw-tooth arrangement of transition metal spins have special interest in the context of zero-energy flat-band modes, similar to those observed in kagome lattices[7]. The presence of such modes imply that, in favourable circumstances, the sawtooth lattice can develop complex magnetic

[3]Hybridization is a process in which two similar magnets are combine to form a new magnet/magnetic field.

ground states rather than conventional ordered ones. The flat-band systems offer promises for dissipation-less propagation of different types of waves[8]. The main interest in the sawtooth lattice originated as a theoretical aspect, in studying the excitation in a Δ chain of $S = 1/2$ spins[9]. Given the importance of sawtooth-based lattices in magnonics, an important emerging field, it is motivating to engage in the search for new sawtooths or detailed re-investigation of less-studied ones. Olivine chalcogenides is a family of compounds which is interesting due to the above-mentioned aspects of sawtooth magnetism and flat electronic and magnonic bands.The ground state of the Δ chain is two-fold degenerate with the spin pairs at the triangular vertices forming a spin-singlet. The spin excitation in the chain is given by a kink-antikink pair which has a dispersionless energy gap[9, 10].

Previous studies indicated a weak ferri or ferromagnetic component exists in a narrow temperature window between 83 K and 86 K, while displaying uniaxial anisotropy with the b direction as the easy axis[1]. The origin of weak ferromagnetism and the unusual temperature dependence of the spin-flop critical field is unclear in olivines despite evidences from neutron scattering experiments. At 4.2 K a collinear ferromagnetic arrangement of the Mn spins at the two distinct crystallographic positions of $4a$ (a site with inversion symmetry) and $4c$ (mirror symmetry), was observed along the b axis. As the temperature increases to 83 K, the orientation of the $4a$ spins turns in the ab plane. At 83 K, both the $4a$ and the $4c$ spins reorient along the a axis but with some canting in the ac plane. It is in the very small temperature range of 83-86 K that spins at two different crystallographic positions display weak ferromagnetism. The paramagnetic to antiferromagnetic transition was identified as belonging to the Heisenberg universality class and the weak ferromagnetic transition as first order with a latent heat approximately 0.01 J/mol[11]. It is also reported that a very low value of magnetic entropy, about 5% of $Rln(2S+1)$, is found to be released at the antiferromagnetic transition, indicating that the spin entropy is not completely removed at the T_N. In addition, purely magnetic intensity was observed in neutron diffraction data measured up to 140 K[1].

In this thesis we first present synchrotron X-ray based analysis of long and short-range structure of the two compounds. The local structure is characterized through pair-distribution function analysis. Further, we present the nuclear and magnetic structures of both the compounds, determined through time-of-flight neutron diffraction experiments. The magnon dispersion of the two olivines are presented for the first time through inelastic neutron scattering experiments. We then present the results from bulk measurements of magnetic susceptibility, and specific heat, $C_p(T)$, of Mn_2SiS_4 and Mn_2SiSe_4 through which we identify the magnetic phase transition temperatures.

Chapter 2

Experimental methods

This chapter discusses solid-state synthesis, the physics behind X-ray diffraction, synchrotron X-ray diffraction techniques, neutron powder diffraction, magnetic susceptibility, and specific heat of solids.

2.1 Solid-state synthesis

Solid-state synthesis, often known as the ceramic method, is a chemical reaction that results in the formation of a new solid with a well-defined structure from solid starting elements[2]. Polycrystalline materials, single crystals, glasses, and thin-film materials are examples of end products that are widely used in energy and electronic applications[2]. The ceramic method, which involves grinding powders of oxides, carbonates, oxalates, or other compounds containing the relevant metals and heating the mixture at a specified temperature after pelletizing the material, is the most popular way of creating metal oxides and other solid materials. This process has been used to make a variety of oxides, sulfides, phosphides, and other chemicals. Even when the reaction is nearly complete, it might be challenging to generate compositionally uniform products using the ceramic approach. Despite these constraints, ceramic techniques have been utilized to successfully synthesize a wide range of solid materials.

$Mn_2SiS_{4-x}Se_x$ ($x = 0$-4) was formed by reacting the elements Mn, Si, S, and Se (99.99%, Aldrich). Prior to pelleting and loading into a 10 mm diameter quartz ampule in a N_2-filled glove box, stoichiometric amounts of these elements were carefully measured, mixed, and weighed using a mortar and pestle. A dynamic vacuum with a pressure less than 10^{-3} mTorr was used to flame-

seal the quartz tubes. The reaction mixtures were heated at a temperature of 1000°C for 24 hours before being cooled at a rate of 100°C/h to room temperature. Samples were re-ground, pelleted, and annealed under the same conditions as required to enhance the phase purity and crystallinity. The removal of oxygen from silica is thought to be aided by iron particles. In a reducing atmosphere, the iron oxide generated in such a reaction would easily be reduced back to metal particles.

The sol–gel method is another technique for making solid materials out of tiny molecules. Metal oxides, particularly those of silicon (Si) and titanium (Ti), are made using this approach (Ti). The method entails converting monomers into a colloidal solution (sol), which serves as a precursor for forming an integrated network (or gel) of discrete particles or network polymers. Metal alkoxides are common precursors.

The sol–gel process leads to the creation of a gel-like network with both a liquid and solid phase. Metal alkoxides and metal chlorides are common precursors, which are converted to colloid through hydrolysis and polycondensation processes. From tiny colloidal particles to continuous chain-like polymer networks, the solid phase's basic structure or morphology can vary greatly[12].

2.2 Crystal structures

Solid state chemistry is primarily concerned with the synthesis, structures, characteristics, and applications of crystalline inorganic materials[2]. Crystal structures and crystal chemistry are ideal places to start. Data on unit cells, their size, and the locations or atomic coordinates of atoms within the unit cell contain all relevant crystal structure information. This basic structural information is combined with knowledge about the elements, their primary oxidation states, ionic radii, coordination requirements, and preferences for ionic/covalent/metallic bonding in crystal chemistry. A working knowledge of the periodic table and element properties is, of course, necessary to appreciate crystal chemistry, but knowledge of crystal structures, particularly crystal chemistry, is a highly useful method to obtain a better understanding of the elements and their compounds.

2.2.1 Crystal systems

We can construct unit cells of various shapes by dividing space by three sets of planes, depending on how the planes are arranged[13]. The unit cell is cubic, for example, if the planes in the three sets are all equally spaced and mutually perpendicular. The vectors a, b, and c[1] in this case are all equal and at right angles to each other, or $a = b = c$ and $\alpha = \beta = \gamma = 90°$[2]. Because the points of the lattice are positioned at the cell corners, we can build unit cells of various forms and hence various types of point lattices by giving special values to the axial lengths and angles. It turns out that all of the potential point lattices can be represented by only seven different types of cells. These correspond to the seven crystal systems that can be used to categorize all crystals. Table 2.1 contains a list of these systems.

Seven different point lattices can be obtained simply by putting points at the corners of the unit cells of the seven crystal systems. Bravais, a French crystallographer, focused on this subject and established in 1848 that there are only fourteen possible point lattices and no more; we refer to this crucial result as Bravais lattice and point lattice as synonymous [13]. For instance, if a point is placed at the center of each cell of a cubic point lattice, the new array of points also forms a point lattice. A cubic unit cell with lattice points at each corner and in the center of each face can also be used to create another point lattice. Table 2.1 and Figure 2.2.1 show the fourteen Bravais lattices, with the symbols P, F, I, and so forth.

To begin, we must distinguish between simple (or primitive) cells (symbol P) and nonprimitive cells (any other symbol): primitive cells have just one lattice point per cell, whereas nonprimitive cells have multiple. A lattice point in a cell's interior "belongs" to that cell, whereas one on the cell face is shared by two cells and one at the corner is shared by eight. As a result, the number

[1] a, b and c are lattice parameters (the length of the lattice).
[2] α, β and γ are inter-axial angles, lattice parameters between a, b and c.

of lattice points per cell is given by

$$N = N_i + \frac{N_i}{2} + \frac{N_c}{8} \tag{2.1}$$

where N_i denotes the number of inner points, N_f denotes the number of points on the face, and N_c denotes the number of points on the corner. Any cell with only lattice points on the corners is considered primitive, but one with additional points in the interior or on faces is considered nonprimitive.

Table 2.1: Crystal systems and Bravais lattices

System	Axial lengths and angles	Bravais lattice	Lattice symbol
Cubic	Three equal axes at right angles $a = b = c, \alpha = \beta = \gamma = 90^\circ$	Primitive Body-centered Face-centered	P I F
Tetragonal	Three axes at right angles, two equal $a = b \neq c, \alpha = \beta = \gamma = 90^\circ$	Primitive Body-centered	P I
Orthorhombic	Three unequal axes at right angles $a \neq b \neq c, \alpha = \beta = \gamma = 90^\circ$	Primitive Body-centered Base-centered Face-centered	P I C F
Rhombohedral/Trigonal	Three equal axes,equally inclined $a = b = c, \alpha = \beta = \gamma \neq 90^\circ$	Primitive	P
Hexagonal	Two equal coplanar axes at 120°, third axis at right angles $a = b \neq c, \alpha = \beta = 90^\circ, \gamma = 120^\circ$	Primitive	P
Monoclinic	Three unequal axes one pair not at right angles $a \neq b \neq c, \alpha = \gamma = 90^\circ \neq \beta$	Primitive Base-centered	P C
Triclinic	Three unequal axes,unequllay inclined and none at right angles $a \neq b \neq c, \alpha \neq \beta \neq \gamma \neq 90^\circ$	Primitive	P

2.2.2 Symmetry

Both Bravais lattices and the real crystals formed on top of them have different types of symmetry. A body or structure is considered to be symmetrical when its constituent elements are structured in such a way that specific operations could be done on it to bring it into alignment with itself. These are termed symmetry operations. For example, if a body is symmetrical in relation to a plane that passes through it, then reflection of either half of the body in the plane, as in a mirror, will produce a body that is identical to the other half.

2.3 X-ray diffraction

2.3.1 Scattering by an electron

The scattering phenomenon begins with electron in the atom[13]. The X-ray tube, which emits X-rays due to the fast deceleration of electrons reaching the target, is a good illustration of this phenomena. Similarly, during its journey, an electron set into oscillation by an X-ray beam accelerates and decelerates continually, emitting an electromagnetic wave. A beam of X-rays that an electron scatters is just the beam that the electron emitted while being hit by the incident beam.

X-rays collide with an electron in the atom and are scattered isotropically. This was studied by the discoverer of electron J.J Thomson[14]. And his equation is given by:

$$I_p = I_o \frac{K}{r^2} \frac{(1 + \cos^2 2\theta)}{2} \tag{2.2}$$

where I_p is intensity of scattered beam at P, I_o is the intensity of incident beam at O, K is constant, r is distance of P from O and 2θ scattered angle between transmitted and scattered beam, refer Figure 2.3.1. From Figure 2.3.1 intensity of the diffracted beam from an electron varies as a function of 2θ. The factor $(\frac{(1+\cos^2 2\theta)}{2})$ which depends on the angle θ, because the scattered radiation becomes partially polarized, which creates a certain anisotropy in the vibrational directions of the electron, as well as a reduction in the scattered intensity (depending

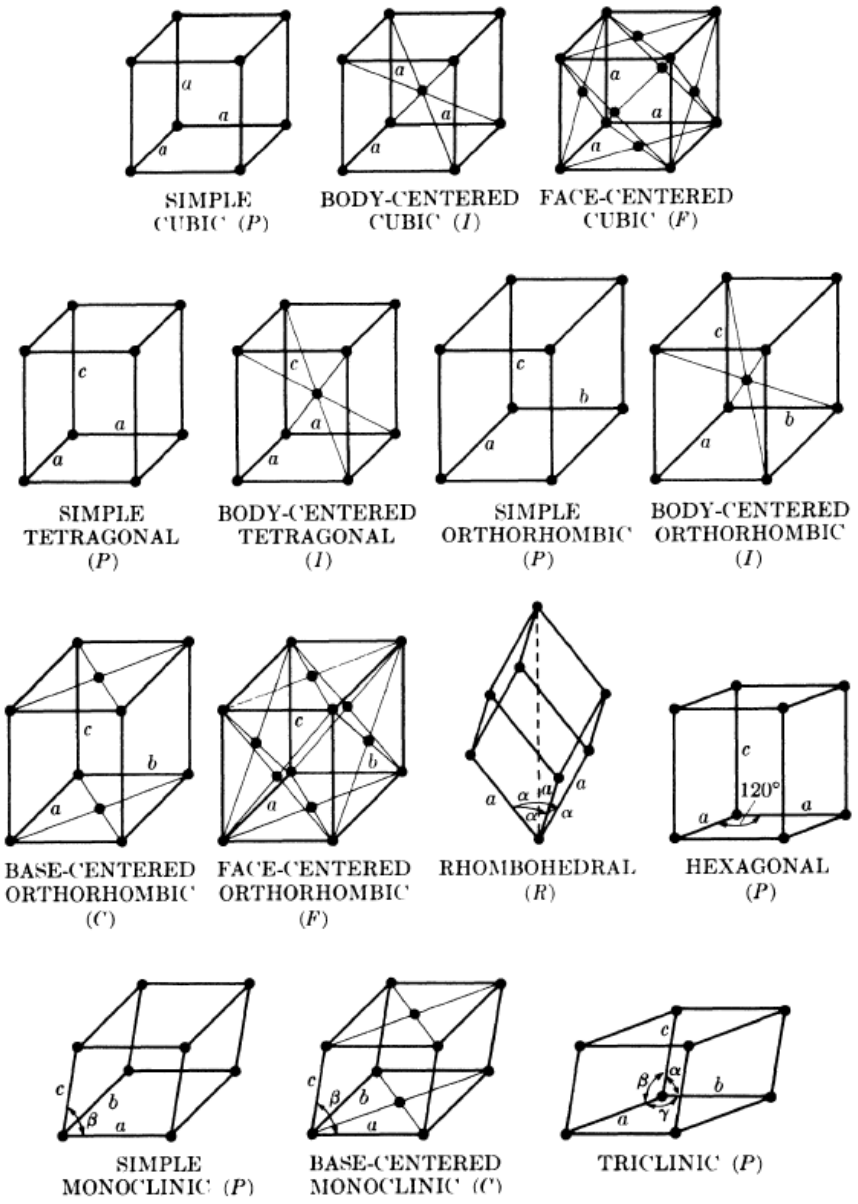

Figure 2.2.1: The fourteen Bravais lattices. Image taken from [13].

of the direction).

2.3.2 Scattering by an atom

When an X-ray beam collides with an atom, each electron scatters coherently a part of the energy, according to the Thomson equation[14]. Because the nucleus has a charge and should be

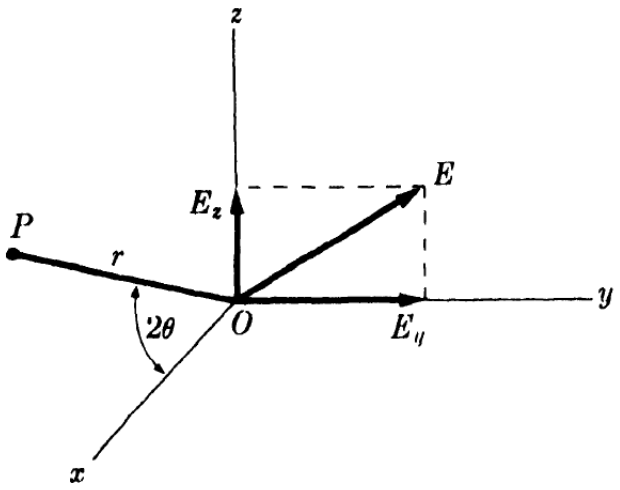

Figure 2.3.1: Scattering of X-rays by a single electron. Image taken from [13]

capable of oscillating under the influence of the incident beam, one may expect it to contribute in coherent scattering as well. However, because the nucleus has a large mass in comparison to the electron, it cannot be made to oscillate to any great extent; in fact, the intensity of coherent scattering is inversely related to the square of the scattering particle's mass, as shown by the Thomson equation. The ultimate result is that an atom's coherent scattering is attributed only to its electrons. An atom with the atomic number Z, scatters a wave with Z times the amplitude of the wave scattered by a single electron. This is because if the scattering is in the forward direction ($2\theta = 0$), all of the atom's electrons' waves will be in phase, and the amplitudes of all the scattered waves can be summed. The efficiency of scattering of a particular atom in a given direction is described by a quantity f, the atomic scattering factor. It's a ratio of amplitudes:

$$f = \frac{\text{amplitude of the wave scattered by an atom}}{\text{amplitude of the wave scattered by one electron}} \tag{2.3}$$

As θ increases, the waves scattered by individual electrons become increasingly out of phase, and f drops. f is also affected by the wavelength of the incident beam: if θ is constant, f will be smaller as the wavelength of the incident beam becomes shorter.

The study of X-rays has a close connection with the study of crystal structure. When Ger-

man physicist von Laue took up the subject in 1912, he was the first to tackle it. He reasoned that if crystals were made up of regularly spaced atoms that could act as X-ray scattering centers, and if X-rays were electromagnetic waves with wavelengths roughly equivalent to the interatomic spacing in crystals, then diffracting X-rays using crystals should be possible. Experiments were carried out under his direction to test this hypothesis: a copper sulfate crystal was placed in the path of a narrow beam of X-rays, and a photographic plate was set up to record the presence of diffracted beams, if any [13]. The first experiment was a success, proving that X-rays were diffracted off of the original beam by the crystal, forming a pattern of spots on the photographic plate. These experiments demonstrated both the wave nature of X-rays and the periodicity of atoms within a crystal at the same time.

The diffraction of X-rays by crystals is similar to reflection of visible light by mirrors. The planes of atoms appear to be small mirrors that reflect the X-rays. However, diffraction and reflection are fundamentally different in at least three ways:
(1) Each crystal atom along the direction of the incident beam scatters a certain number of rays, which combine to form the diffracted beam from a crystal. Only a small portion of the surface reflects visible light. (2) Only incidence angles that follow the Bragg law enable monochromatic X-rays to diffract (discussed below). Any angle of incidence can allow visible light to reflect. (3) Nearly all of the light that can be seen is reflected by a good mirror. A diffracted X-ray beam's intensity is minimal in comparison to the incident X-ray beam. Figure 2.3.2 shows that there wouldn't be a diffraction if only a small amount of X-ray absorption and transmission were occurring in the crystal. In the absence of diffraction, only transmission beams or a central spot should have been seen. Diffraction, in general, is a scattering phenomenon that happens when a large number of atoms interact with one another. The periodic arrangement of the atoms on the lattice gives rise to definite phase relations between the rays that are scattered by them; these phase relations are such that destructive interference occurs in the most of of scattering directions, whereas constructive interference occurs in a small number of directions, leading to diffracted beams.

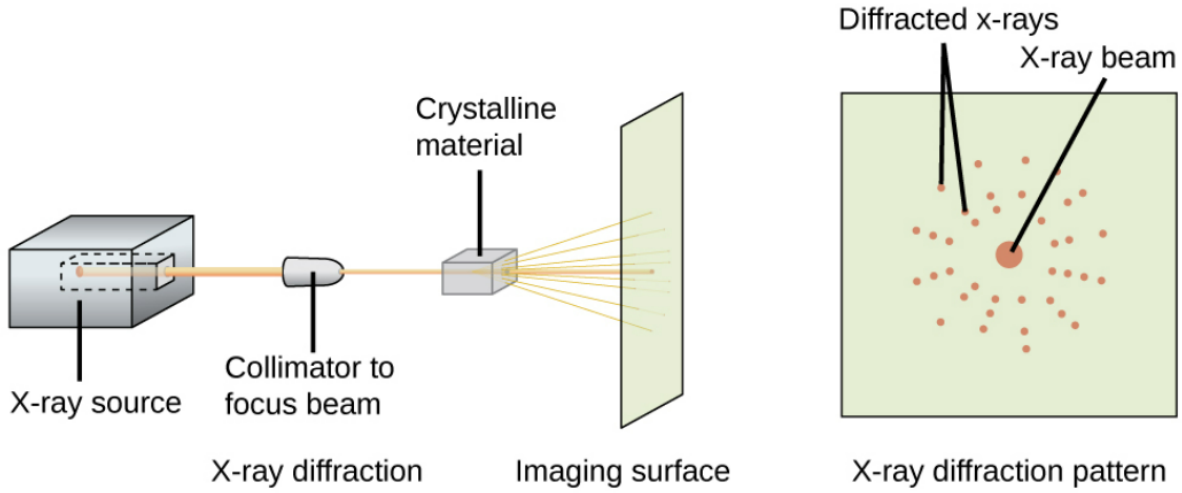

Figure 2.3.2: In a diffractometer, a beam of X-rays strikes a crystalline material (left image), producing an X-ray diffraction pattern that can be analyzed to determine the crystal structure (right image). Image taken from [15].

X-rays are very energetic electromagnetic rays with an energy ranging from 200 eV to 1 MeV. X-rays are produced in an X-ray tube when accelerating electrons hit a target anode it starts to decelerating and loosing energy results a release of an electromagnetic radiation which identified as an X-ray. X-ray powder diffraction is an effective technique which gives information about a crystal structure and the arrangement of atoms in a crystalline sample. When a monochromatic X-ray arrive on a sample, the intensity of a diffracted X-rays are measured as a function of a scattered angle.

Bragg's law, describes the reflection of X-rays on the surface of imaginary mirrors generated by atomic planes in the crystal lattice (shown in Figure 2.3.3 as horizontal lines containing scattering centers, that is, atoms shown as black circles in the image). Because of the crystal's repeated nature, these planes would be separated by a constant distance d. Mathematically Bragg's law is given by[16];

$$2d \sin\theta = \mathrm{n}\lambda \tag{2.4}$$

where λ is the wavelength of the X-ray, d is the spacing of the crystal layers (path difference), θ is the incident angle (the angle between incident ray and the scatter plane), and n is the diffraction order (an integer). Figure 2.3.4 shows the detector rotates around the sample in a

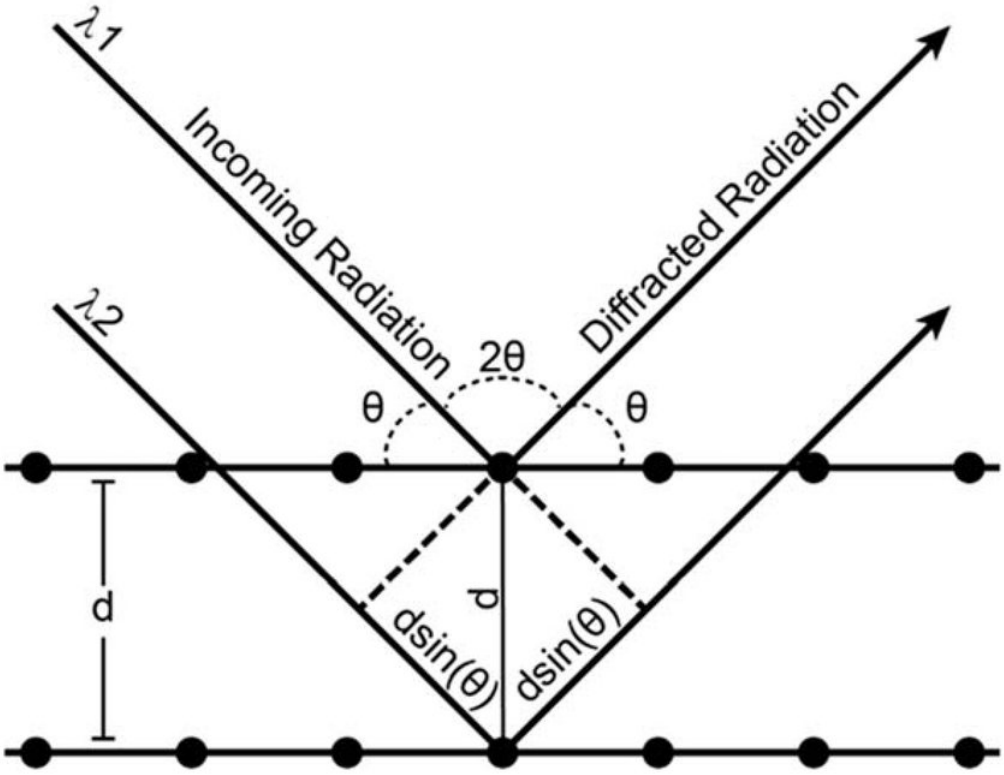

Figure 2.3.3: Bragg's Law: X-rays incident on the crystal at an angle θ produce coherent diffraction (in phase) when the difference in the distance travelled is equal to an integral number of the wavelength (nλ). Figure adapted from[16].

.

circle. The angle (2θ) of the detector position is recorded. The detector keeps track of how many X-ray photons are seen at each angle 2θ. The intensity of X-rays is commonly measured in counts or counts per second. The incident angle ω changes alongside with 2θ to keep the X-ray beam properly focused. Rotating the sample or the X-ray tube is one way to accomplish this.

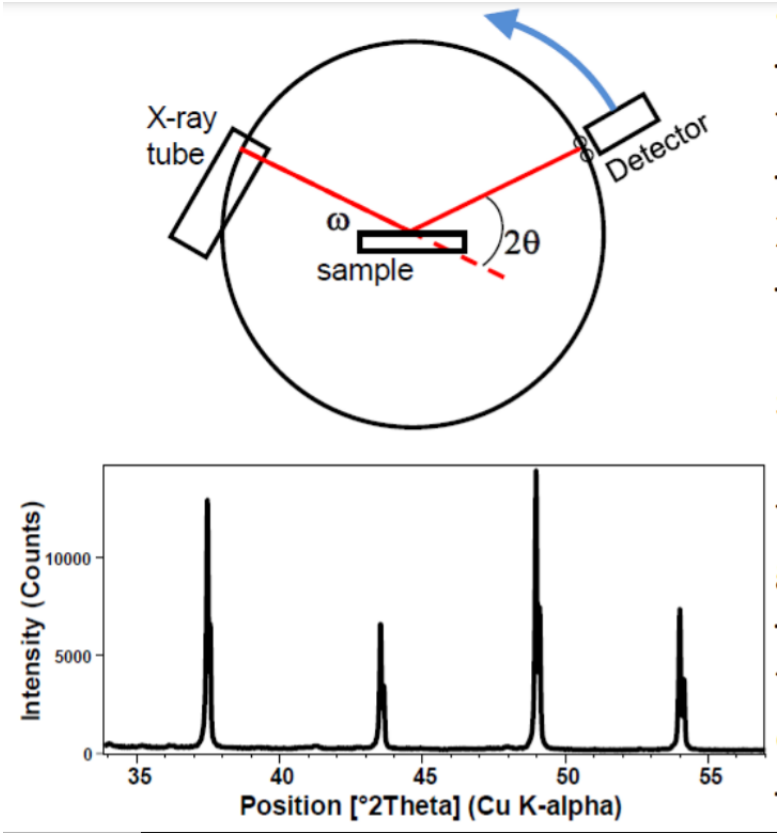

Figure 2.3.4: The detector moves in a circle around the sample and records the number of X-ray photons observed at each angle 2θ (top panel). A plot showing the intensity of X-rays scattered at different angles by a sample which is known to be an X-ray powder diffraction pattern (bottom panel). Image adopted from https://rb.gy/a0m9ea.

2.4 Powder diffractometer

Powder diffraction, when used appropriately, may provide a wealth of structural information about the material being studied. Diffraction of monochromatic X-rays by a powder specimen is the basic principle behind this approach. The strong Kα characteristic component of α radiation from an X-ray tube operating above the K excitation potential of the target materials is commonly referred to as monochromatic in this situation. A crystal monochromator is usually used in diffractometry to exclude all wavelengths except the Kα wavelength. The disadvantage of filters is that transmitted radiation is still not entirely monochromatic and background radiation is still quite high. In reality, single crystals are mosaics made up of many small crystal blocks that are generally aligned in a certain direction. The so-called mosaic spread of the crys-

tal is determined by the distribution of block alignment. Pyrolytic graphite and silicon are two materials that are commonly employed to make broad band and narrow band monochromators. The basic X-ray diffractometer/spectrometer is actually two instruments, depending on how they are used: an instrument for measuring X-ray spectra with a known structural crystal and for studying crystalline (and noncrystalline) materials by measuring how they diffract (scatter) X-rays of known wavelength.

The intensity of a diffracted beam is measured by a diffraction camera by the amount of blackening it creates on photographic film, which requires a microphotometer measurement of the film to convert amount of blackening into X-ray intensity. An electronic X-ray detector measures the intensity of a diffracted beam directly from the diffractometer. X-ray detectors come in a variety of shapes and sizes, but they always convert incoming X-rays into electric current surges or pulses that are supplied into various electronic components, including computers, for processing. The electronics count the number of current pulses per unit of time, which is proportional to the X-ray beam's intensity when it enters the detector. A diffractometer is similar to a Hull/Debye Scherrer camera, except that instead of a strip of film, a moveable detector is used. The X-ray detector or film is mounted on the circumference of a circle centered on the powder specimen in both instruments, which uses practically monochromatic radiation.

2.5 Powder diffraction at Advanced Photon Source (APS)

Powder diffractometers are dedicated devices that are optimized for collecting diffraction patterns. The term "optimized" refers to the ability to capture the pattern as quickly as feasible, or with the highest possible Q-resolution [17]. Synchrotron X-ray diffraction is one of the techniques used to aquire detailed structural data about a particular material[18]. This method is based on Bragg's law, which implies that interference that is in phase produces constructive interference and interference that is out of phase produces destructive interference.

An engineering model of the 11-BM diffractometer at APS is shown in Figure 2.4.1. The

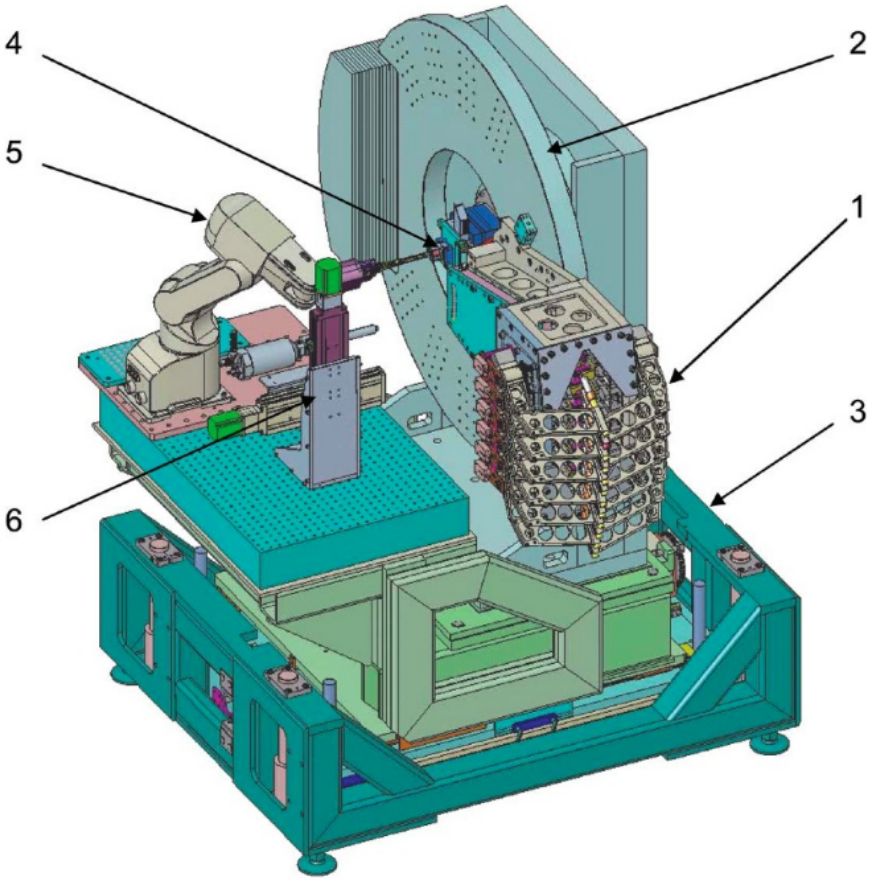

Figure 2.4.1: Schematic diagram of X-ray diffractometer. A three-dimensional model of the high-resolution diffractometer with 12 analyzer detector system: (1) 12-analyzer detector system, (2) two-circle goniometer, (3) supporting table, (4) sample stages, (5) sample mounting robot, (6) stages for cryostream. Image taken from https://rb.gy/iaet9n.

12-analyzer detection system (1) is installed on the main circle of a high-resolution two-circle diffractometer (2) made up of customized Huber GmbH 480 and 420 goniometers. The diffractometer measures 2600 mm (h)×2100 mm (l)×1700 mm(w) and comes with a three-dimensional adjustable supporting table (3), with all 12 analyzers fitting within the space limited by the radius of the main goniometer, the 12-analyzer detector system achieves a 2 degree separation between surrounding analyzers. The 12 analyzers and detectors are divided into two types of subassemblies to address this technical challenge: six left-side units and six right-side units. The interleaved analyzer crystal assemblies that arise are positioned on both sides of the vertical plane defined by the sample center and the incoming X-ray beam direction.

Many experimental factors can limit the amount of information collected from a powder pattern. Signal-to-noise, which is determined by the source intensity and ability to separate diffraction signal from air scatter and fluorescence; measurement range, which is limited by the source wavelength; and poor instrumental resolution, which reduces the number of observable intensity measurements due to the overlap of separate reflections, are some of these effects[19]. By providing a very intense and almost parallel beam of high-energy X-rays, the utilization of a synchrotron source allows all of these constraints to be minimized. Three-crystal diffraction optics (two-crystal monochromation combined with a perfect-crystal analyzer) can be used with this powerful beam to detect diffraction peaks with extremely high resolution. The use of such a crystal analyzer design further improves signal versus background since fluorescence and accidental scatter are rejected.

Debye-Sherrer transmission geometry (with a revolving capillary sample) is commonly used in synchrotron powder diffraction measurements, which helps to avoid problems with sample orientation preference. The triple-crystal optic, on the other hand, is inefficient, and even with a synchrotron source of enormous intensity, a typical scan could take up to a day. As a result, new synchrotron powder diffractometers now have anywhere from 10 to 40 sets of analyser crystals and detectors, allowing for substantially faster data gathering durations of about an hour. The 11-BM is situated at Argonne National Laboratory, APS where the beamlines of synchrotron X-rays are from a bending magnet source[20]. The use of synchrotron source provides a high signal-to-noise ratio and high resolution measurement[19]. The synchrotron X-ray is more preferable since it gives a high sensitivity and helps to observe the weak peaks above the background. It also provides a detailed information of the sample with a wider Q range, the momentum transfer during scattering.

11-BM has the following instrument specifications;

- ✓ The beam line covers an energy range of 15 keV - 35 keV.

- ✓ Beam size of 1.5 mm (horizontal)∗0.5 mm (vertical) focus at the sample.
- ✓ Angular coverage of 2θ range from 0.5°-130°.
- ✓ Resolution of $\frac{\Delta Q}{Q} \approx 1.4 * 10^{-4}$.

Upon loading the sample on to instrument the robotic system will take care of the data collection coded by python. MySQL and EPICS are tools to access the metadata from the database[21]. The strong magnetic fields required to produce synchrotron radiation are generated by a variety of devices. The electrons or positrons are deflected and forced to circulate within the storage ring by bending magnets placed at periodic intervals around the ring. Another source of radiation is insertion devices, which consist of a very closely spaced array of magnets positioned between the bending magnets. Table 2.2 shows list of countries around the world with synchrotron facility[22].

2.6 Pair distribution function analysis

The pair distribution function of a material is derived experimentally by Fourier transformation of a scattering pattern, which reveals direct-space insights into any long-range ordered structure from Bragg scattering (i.e., diffraction) and short-range structural correlations from diffuse scattering intensity. When the samples have defects, disorder, and/or discrete material structures, the atomic pair distribution function (PDF) analysis of diffraction data can fill the gap[23]. A simple 1D function that incorporates information about structural correlations in a material is the atomic pair distribution function, G(r). What is the purpose of this function? To begin with, it is simple to measure experimentally. Second, calculating from a known structure is straightforward. Third, it provides an intuitive local picture of the structure, as if you were sitting on an atom looking out at your surroundings. It is derived simply from the auto correlation function of the atomic density, but it intuitively yields the probability of detecting pairs of atoms separated by r. Within the measurement time and sample volume, the structural signal measured is an average of all local states. G(r) is related to the probability of finding an atom at a distance r from a reference atom. It is the Fourier transform of the total structure factor,

Table 2.2

Country	Name	Website
Armenia	Center for the Advancement of Natural Discoveries using Light Emission	http://www.candle.am/index.html
Australia	Australian Synchrotron	http://www.synchrotron.org.au
Brazil	Laboratorio Nacional de Luz Sincrotron	http://www.lnls.br/
Canada	Canadian Light Source	http://www.lightsource.ca
China	Beijing Synchrotron Radiation Facility	http://bsrf.ihep.cas.cn/
	National Synchrotron Radiation Laboratory	http://www.nsrl.ustc.edu.cn/
	SSRF - Shanghai Synchrotron Radiation Facility	http://ssrf.sinap.ac.cn/english/
Denmark	Institute for Storage Ring Facilities	http://www.isa.au.dk/
France	European Synchrotron Radiation Facility	http://www.esrf.eu
	SOLEIL	http://www.synchrotron-soleil.fr/
Germany	Angstromquelle Karlsruhe - ANKA	http://anka.kit.edu
	BESSY II - Helmholtz-Zentrum Berlin	http://www.helmholtz-berlin.de/
	Dortmund Electron Storage Ring Facility	http://www.delta.tu-dortmund.de/
	ELSA - Electron Stretcher Accelerator	http://www-elsa.physik.uni-bonn.de/elsa-facility_en.html
	Metrology Light Source	http://www.ptb.de/mls/
	PETRA III at DESY	http://photon-science.desy.de
India	Centre for Advanced Technology	http://www.cat.ernet.in/technology/accel/indus/index.html
Iran	Iranian Light Source Facility	http://ilsf.ipm.ac.ir/
Italy	DAFNE	http://web.infn.it/Dafne_Light/
	Elettra Synchrotron Light Laboratory	http://www.elettra.eu
Japan	Aichi Synchrotron Radiation Center	http://www.astf-kha.jp/synchrotron/en/
	Hiroshima Synchrotron Radiation Center	http://www.hsrc.hiroshima-u.ac.jp/index.html
	Photon Factory	http://www.kek.jp/
	Ritsumeikan University SR Center	http://www.ritsumei.ac.jp/acd/re/src/index.htm
	Saga Light Source	http://www.saga-ls.jp/?page=206
	SPring-8	http://www.spring8.or.jp/en/
	Ultraviolet Synchrotron Orbital Radiation Facility	http://www.uvsor.ims.ac.jp/defaultE.html
Jordan	Synchrotron-light for Experimental Science and Applications in the Middle East	http://www.sesame.org.jo/sesame/
Korea	Pohang Light Source	http://paleng.postech.ac.kr
Russia	Dubna Electron Synchrotron	http://wwwinfo.jinr.ru/delsy/
	Kurchatov Synchrotron Radiation Source	http://www.nrcki.ru/e/engl.html
	Siberian Synchrotron Research Centre	http://ssrc.inp.nsk.su/
	TNK	http://www.niifp.ru/page/sinhrotron
Singapore	Singapore Synchrotron Light Source	http://ssls.nus.edu.sg/index.html
Spain	ALBA	http://www.cells.es/
Sweden	MAX IV Laboratory	https://www.maxiv.se
Switzerland	Swiss Light Source	http://www.psi.ch/sls/
Taiwan	National Synchrotron Radiation Research Center	http://www.nsrrc.org.tw/
Thailand	Synchrotron Light Research Institute	http://www.slri.or.th
United Kingdom	Diamond Light Source	http://www.diamond.ac.uk/
France	Centre Laser Infrarouge d'Orsay	http://clio.lcp.u-psud.fr/clio_eng/clio_eng.htm
Germany	European XFEL	http://www.xfel.eu/
	FLASH at DESY	http://photon-science.desy.de
	Free Electron Laser at ELBE	http://www.fzd.de/db/Cms?pNid=471
Italy	FERMI	http://www.elettra.eu/lightsources/fermi.html
Japan	IR FEL Research Center	http://www.rs.noda.tus.ac.jp/fel-tus/
	SPring-8 Angstrom Compact Free Electron Laser	http://xfel.riken.jp/eng/index.html
Switzerland	Swiss Free Electron Laser	http://www.psi.ch/swissfel/swissfel
Netherland	Free Electron Laser for Infrared eXperiments	http://www.ru.nl/felix/
Turkey	TARLA Infrared FEL and Bremsstrahlung Facility	http://www.tarla.org.tr

Table 2.2: Continued...synchrotron-based research facilities around the world, source[22].

USA	Institute for Terahertz Science and Technology	http://www.itst.ucsb.edu/
	Jefferson Lab FEL	https://www.jlab.org/free-electron-laser
	Linac Coherent Light Source	http://lcls.slac.stanford.edu
	Advanced Light Source	http://www-als.lbl.gov/
	Advanced Photon Source	http://www.aps.anl.gov
	Center for Advanced Microstructures and Devices	http://www.camd.lsu.edu/
	Cornell High Energy Synchrotron Source	http://www.chess.cornell.edu/
	National Synchrotron Light Source II	http://www.bnl.gov/ps/
	Stanford Synchrotron Radiation Lightsource	http://www-ssrl.slac.stanford.edu
	Synchrotron Ultraviolet Radiation Facility	http://physics.nist.gov/majresfac/surf/index.html

S(Q). The structure function, S(Q) is related to coherent part of the diffraction intensity and adjusts for the scattering power of atoms and g(r)is the pair distribution function, refer Equation 2.6. Figure 2.6.1 shows atypical PDF. The peak area indicates the number of pairs weighted by scattering power, i.e. coordination number/concentration and the peak width refers to the range of inter atomic distances due to static and dynamic disorder. For more detailed explanation on PDF see Section 3.

$$G(r) = 4\pi r \rho_0 [g(r) - 1] \tag{2.5}$$

$$= \left(\frac{2}{\pi} \int Q[S(Q) - 1] \sin(Qr) dQ \right) \tag{2.6}$$

2.7 Neutron scattering

In 1945, Ernest O. Wollan used the Graphite Reactor at Oak Ridge to conduct the first neutron diffraction studies[25]. Clifford Shull joined him shortly after (June 1946) [26], and together they established the basic concepts of neutron scattering and successfully applied it to a variety of materials, addressing issues such as the structure of ice and the microscopic arrangements of magnetic moments in materials. Shull received half of the Nobel Prize in Physics in 1994 for this achievement[27]. The neutron has a number of properties that make it an excellent probe for studying atomic structure and motion. They are listed here in no particular sequence. The neutron only has very weak interactions with materials since it has no electric charge. In other

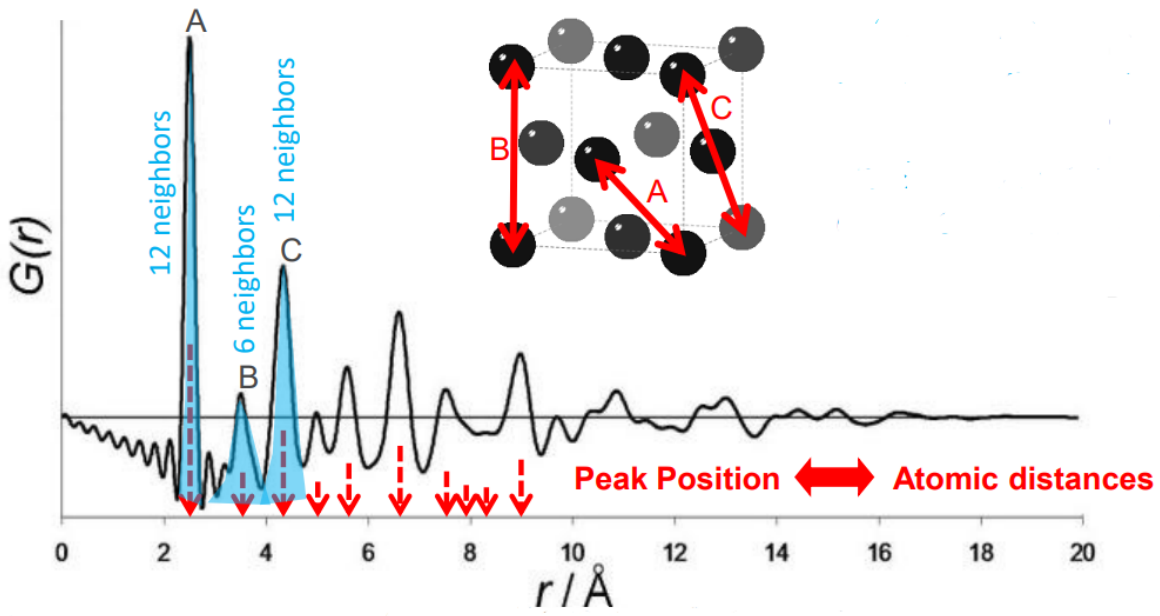

Figure 2.6.1: Schematic diagram commonly used for pair distribution functions G(r). G(r) is related to the probability of finding an atom at a distance r from a reference atom. Image taken from [24].

words, a neutron has a higher probability of passing through a substance than it does of not. This is advantageous since it means that neutrons illuminate materials extremely uniformly; neutrons can scatter from anywhere in the sample, rather than only from the surface as in typical light scattering. As a result, neutrons are known as a bulk probe [17]. The use of neutron scattering to determine a material's atomic and/or magnetic structure is referred to as neutron diffraction or elastic neutron scattering.

The Spalliation Neutron Source (SNS) is an Oak Ridge National Laboratory (ORNL) facility that is comprised of a 1-GeV linear accelerator ion source and a proton accumulator ring that delivers a 1.4-MW beam to a liquid mercury target. Three main types of accelerators are used in the linear accelerator to accelerate hydrogen beams from 2.5 to 1000 MeV, or 1 GeV. A drift tube and a linked cavity linear accelerator, both made of copper and operating at room

temperature, are also used before the superconducting linear accelerator. A short, sharp pulse of electrons is required for optimal neutron scattering research, and this is achieved by compressing the H-beam from the linear accelerator by more than 1000 times.

A sample is immersed in a beam of hot (thermal neutron)[3] or cold neutrons[4] to produce

Figure 2.7.1: An image of the POWGEN detector taken from the ORNL website[28].

a diffraction pattern that reveals the material's structure. Although similar to X-ray diffraction, neutrons and X-rays provide complimentary information because to their differing scattering properties: X-rays are best for surface analysis, while synchrotron-produced strong X-rays are best for shallow depths or thin specimens, and neutrons with a deep penetration depth are best for bulk materials[29].

Diffraction of neutrons is an extremely expensive technology. A nuclear reactor is required to obtain a sufficiently intense neutron source. Few laboratories have their own neutron facility, thus experiments are conducted at central laboratories that provide a user service (e.g. at the ILL, Grenoble, France, the Rutherford-Appleton Laboratory, UK, and the Argonne Laboratory, USA)[2]. Because neutron beams are typically low in intensity, the sample size required for

[3]Thermal neutron is a free neutron with a kinetic energy of about 0.025 eV.

[4] Cold neutrons are very low energy (5×10^{-5} eV to 0.025 eV) neutrons in a reactor, used for research into solid-state physics because it has a wavelength of the order of crystal lattice spacings and can therefore be diffracted by crystals.

diffraction investigations is relatively big, at least 1 mm^3. Because large crystals are rarely available, crystallographic studies are usually performed on polycrystalline samples.

Unlike X-rays, neutrons are scattered predominantly by atomic nuclei. Neutrons are also scattered by the interaction of the neutron magnetic moment with the magnetic moment(s) of the atoms in the case of magnetic materials. In both X-ray and magnetic neutron scattering, the scattering object (i.e. the electron dispersion) is comparable in size to the wavelength of the X-rays or neutrons.

2.8 Scattering cross-section

The ability of the target atoms to deflect incident neutrons is referred to as the neutron scattering cross-section. The ratio of neutrons scattered by the target atoms per second to neutrons incident per unit area per second can be used to characterize it (incident neutrons flux). Figure 2.9.1 shows the scattering geometry. The sample (target) scatters an incident neutron of wavevector k, and the scattered wave is recorded by a neutron detector at a location determined by the polar angles θ, ϕ and subtending a solid angle $d\Omega = \sin\theta d\theta d\phi$. The scattered neutron flux measured by the detector for an incident neutron flux of N (neutrons per second per unit area) is given by; $N\left(\frac{d\sigma}{d\Omega}\right)d\Omega$. The differential scattering cross section $\frac{d\sigma}{d\Omega}$ is defined by this formula. At this point, we've assumed that the scattering nucleus is locked in place and that no energy is transferred between the nucleus and the neutron, implying that the scattering is totally elastic. The scattered wave can be represented by the spherical wave $\psi = -(\frac{b}{r})e^{ikr}$ if the incident neutrons have a plane wave $\psi = e^{ikr}$. Where r is the distance between the scattering nucleus and the detector, and $k = \frac{2\pi}{\lambda}$ is the wave number. In neutron diffraction, the constant b, also known as the scattering length, is a very important variable. It is the neutron equivalent of the X-ray scattering factor or form factor (f), and it has the dimensions of length. The total scattering cross section can be found by integrating the differential cross section with respect to solid angle($d\Omega$);

$$\begin{aligned} \sigma = & \text{ flux of scattered neutrons/incident flux} \\ = & \ 4\pi r^2 v \frac{|-(\frac{b}{r})e^{ikr}|^2}{|ve^{ikr}|^2} \\ = & \ 4\pi b^2 \end{aligned} \tag{2.7}$$

v is the velocity of neutrons. The imaginary part of the scattering length b is responsible for neutron absorption. Fortunately, most elements and isotopes have a low absorption coefficient, therefore b can be considered a true constant. Neutron-shielding materials such as Cd, Gd, and B are notable exceptions. The real and imaginary components can be treated independently as the scattering cross section (σ_s) and the absorption cross section (σ_a) in diffracted intensities.

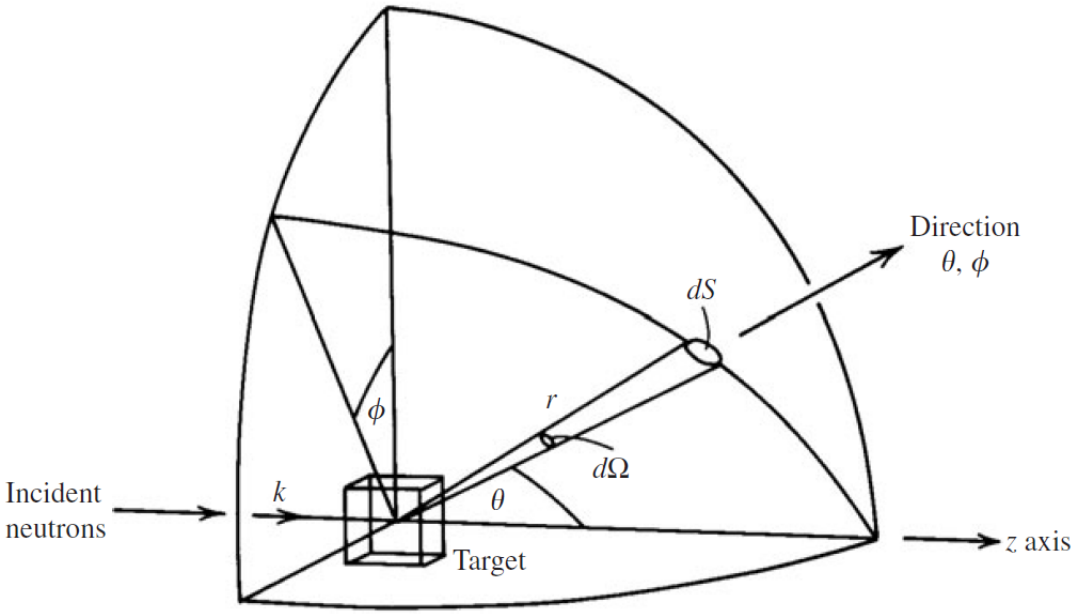

Figure 2.8.1: Geometry of a neutron scattering experiment[30]

.

2.8.1 Coherent and incoherent scattering

Coherent scattering occurs when all atoms scatter in the same way. We call it incoherent scattering when we can only see what individual atoms are doing. Thus, while coherent scattering provides information about atom relative positions and collective motions such as sound waves, incoherent scattering provides information about individual atom motions such as diffusion through a liquid. Coherent scattering is always present in X-ray scattering. This is because photons are scattered by electrons around nuclei, and each electron has the same scattering strength as every other electron. Thus, X-ray scattering will not reveal an isotope effect (because all isotopes have the same number of electrons) or a nucleus effect (since the nucleus is not what scatters the photons). There will obviously be variations in the scattering potential around some mean value in any atom arrangement. These can occur as a result of human action (alloying or doping), by chance (impurity atoms), or as an unavoidable feature of the system (isotopic mixture and distribution of nuclear spins). The differential scattering cross section is given by the following expression based on the scattering from a system with a random distribution of scattering nuclei[30]. The differential scattering cross section can be expressed as follows:

$$\begin{aligned} \frac{d\sigma}{d\Omega} &= |\bar{b}|^2 \left| \sum \exp(ik.r_n) \right|^2 + N|\overline{b-\bar{b}}|^2 \\ &= \left(\frac{d\sigma}{d\Omega}\right)_{\text{coherent}} + \left(\frac{d\sigma}{d\Omega}\right)_{\text{incoherent}} \end{aligned} \tag{2.8}$$

where $|\bar{b}|^2 \left| \sum \exp(ik.r_n) \right|^2$ is $\left(\frac{d\sigma}{d\Omega}\right)_{\text{coherent}}$ and $N|\overline{b-\bar{b}}|^2$ is $\left(\frac{d\sigma}{d\Omega}\right)_{\text{incoherent}}$, also $\bar{b}$ is the mean scattering length for all atoms in the system, k is the scattering vector (difference in wave vector of scattered and incident neutrons, r_n is the position vector of the n^{th} atom in the system, and N is the number of atoms in the system.

To investigate the magnetic structures of sawtooth olivines Mn_2SiX_4 (X = S, Se) using neutron powder diffraction, measurements were carried out in the temperature range 1.8 K to 300 K at POWGEN instrument[28] located at Oak Ridge National Laboratory. Data from this dif-

fractometer is weel-suited for Rietveld analysis[31] because it is a significantly high resolution measurement. Some of this resolution can be traded for intensity, allowing for shorter measurements with high resolution. With the help of FULLPROF software[32], we examine the magnetic structure based on this measurements. We conducted diffraction experiments using central wavelengths 1.5 Å and 2.66 Å.

2.9 Magnetic scattering

Until now, we've solely dealt with nuclear scattering. The neutron's magnetic moment also permits it to interact with atoms' orbital and spin magnetic moments in a solid. Although only a small fraction of elements carry such magnetic moments, the vector nature of these magnetic moments ensures a vast array of possible magnetic structures and causes magnetic scattering to be a vector process, rendering a simple scalar scattering length insufficient.

Unpaired electron spins are what cause magnetic scattering from a single atom (or ion). Interference effects occur because the scattering object, the electron distribution, is similar in size to the wavelength of thermal neutrons, resulting in a magnetic form factor[30]. For an ordered magnetic structure, we can write the differential magnetic neutron scattering cross section per atom as follows:

$$\left(\frac{d\sigma}{d\Omega}\right)_{\text{mag}} = q^2 S^2 \left(\frac{e^2\gamma^2}{m_e c^2}\right)^2 f^2 \tag{2.9}$$

where, q is the magnetic interaction vector, S is spin quantum number of target atom, e and m are the charge and mass of the electron respectively. Also, c is speed of the light, γ is the magnetic moment of the neutron and f represents magnetic form factor. Magnetic scattering is coherent and produces strong diffraction effects when the atomic magnetic moments are closely correlated, as in ordered magnetic structures. Similarly to how we defined a coherent scattering length b_{coh} in the topic of coherent nuclear scattering, we define the magnetic scattering length

as follows:

$$p = \left(\frac{e^2\gamma^2}{2m_e c^2}\right) gJf \tag{2.10}$$

Here g is Lande splitting factor and J is total angular momentum.

The interaction of magnetic scattering with nuclear scattering is an important factor to consider. Because magnetic scattering is vector, it is highly dependent on the polarization of the incident neutron beam. There are five terms that make up the overall cross section:

$$\sigma_{\text{tot}} = \sigma_{\text{coh}} + \sigma_{\text{incoh}} + \sigma_{NM} + \sigma_{\text{M}} + \sigma_{\text{pol}} \tag{2.11}$$

where σ_{coh} and σ_{incoh} are the previously defined coherent and incoherent nuclear scattering cross sections, σ_{NM} is the nuclear–magnetic interference term, σ_M is the magnetic scattering cross section (eqn 2.9), and σ_{pol} is the polarization-dependent term, and σ_{NM} is the nuclear–magnetic interference term. If incoherent scattering is ignored and only simple magnetic structures with co-linear moments are considered, the differential cross section becomes:

$$\frac{d\sigma}{d\Omega} = b^2 + 2bp\hat{\mathbf{P}}.\mathbf{q} + p^2q^2 \tag{2.12}$$

where $\hat{\mathbf{P}}$ is a unit vector specifying the incident neutron beam's polarization direction. The pure polarization terms σ_{pol} are zero in this very simple structure, leaving only the nuclear, magnetic, and nuclear–magnetic interaction terms. The interaction term averages to zero if the incident neutron beam is unpolarized (i.e. $\hat{\mathbf{P}}$ can take any orientation), thus we have left;

$$\frac{d\sigma}{d\Omega} = b^2 + p^2q^2 \tag{2.13}$$

2.9.1 The intensity of diffracted beams from an ideal polycrystalline material

We considered the crystal as though it were made up of ideal surfaces with uniform scattering density when analyzing diffraction from it. It isn't necessarily the case. First, the scattering density is concentrated among atoms (or nuclei in the case of nuclear neutron diffraction) with different scattering lengths, and second, there are relatively few flat planes of atoms in any but the simplest structures. The phase difference between pairs of light atoms is 2π or $= 0$ at the

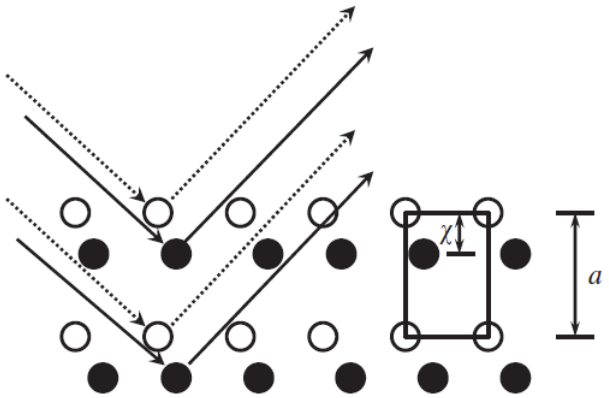

Figure 2.9.1: Diffraction from a simple two-dimensional structure, two atoms (open and filled circle). a is unit cell parameter and χ, the coordinate of the dark atom [30].

Bragg angle for diffraction from the planes of atoms illustrated. The phase difference between the two dark atom pairs is also 2π or $= 0$, refer to Figure 2.9.1. However, because the phase difference between subsequent rows of dark and light atoms is $2\pi hx(x = \chi/a)$, leading to some cancellation and reduced intensity of the scattered wave and x is the path difference. In general, the phase of a wave scattered by a dark atom (shaded circle) in three dimensions compared to a wave scattered by a light atom (open circle) at the origin is

$$\phi = 2\pi(hx + ky + lz) \tag{2.14}$$

where (x, y, z) is co-ordinate of the atom with dimensions a, b, c and h, k, and l are the Miller indices. Consider the bright and dark atoms shown in Figure 2.9.1. The wave scattered by a

certain atom can thus be written as;

$$Ae^{i\phi} = be^{2\pi i(hx+ky+lz)} \tag{2.15}$$

where, A is the amplitude of the scattered wave and the structure factor (F) is given by;

$$F_{\text{hkl}} = \sum_n b_n e^{2\pi i(hx_n+ky_n+lz_n)} \tag{2.16}$$

By writing the position vector of the n^{th} atom as r_n and we have

$$F_{\text{hkl}} = \sum_n b_n e^{2\pi i(H_{hkl}r_n)} \tag{2.17}$$

Equations 2.16 and 2.17 are the Fourier transforms of the crystal structure sampled at the reciprocal lattice points. H_{hkl} is a reciprocal space vector and always perpendicular to the real space plane defined by the Miller indices, (hkl).

2.10 Magnetic susceptibility

Any substance's atoms have an electronic structure that involves electrons circulating in orbits around a central nucleus. Because electrons have an electrical charge, their movement creates an electrical current, which causes each electron to produce a magnetic moment. Furthermore, due to their spin, all electrons have magnetic moments.

Because the orbital and spin components cancel out, many elements' atoms have zero magnetic moments. When such atoms are placed in a magnetic field, the spin and orbital motions of their electrons are rearranged, resulting in a net magnetic moment in the opposite direction of the field. Diamagnetism is the term for this type of behavior.

The magnetic susceptibility (Latin: susceptibilis, "receptive"; indicated in electromagnetism) is a measure of how much a substance will get magnetized in the presence of a magnetic field.

The magnetic moment per unit volume, or magnetization, is measured as a ratio to the applied magnetic field intensity, or H.

$$\chi = \frac{M}{H} \tag{2.18}$$

This simplifies the classification of most materials' responses to a magnetic field into two categories: alignment with the magnetic field $\chi > 0$, which is known as paramagnetism, and alignment against the field $\chi < 0$, which is known as diamagnetism.

A material's magnetic susceptibility determines whether it is attracted to or repelled from a magnetic field. Paramagnetic materials align themselves with the applied field and are drawn to areas with a higher magnetic field. Anti-aligned diamagnetic materials are driven away from lower magnetic field locations. The material's magnetization adds its own magnetic field on top of the applied field, causing field lines to concentrate in paramagnetism or be excluded in diamagnetism.

2.10.1 Measuring magnetic susceptibility

To properly define a material's bulk magnetic characteristics, magnetic susceptibility is commonly assessed using a variety of applied magnetic field strengths and over a range of temperatures. A vibrating sample magnetometer (VSM) equipped with a superconducting quantum interference device pick-up coil (SQUID) is used to detect magnetic susceptibility[33]. Magnetic measurements, high conductivity materials, and magnetic field measurements are only a few of the uses for the VSM. Magnetic susceptibility is measured as a function of temperature while the sample is heated in zero field cooled (ZFC) where the sample was cooled without any applied magnetic field, it is a reversible process. Field cooled (FC) measurements are done when the sample is cooled under the same magnetic field, this process is not a reversible.

2.10.2 Curie and Curie–Weiss laws

Above a temperature known as the Curie temperature, T_C (ferromagnets), or the Neel point, T_N (antiferromagnets), ordered magnetic structures lose their ordered structures, and the materials become paramagnetic. There is a balance at these transition temperatures between thermal energy, which seeks to randomize the orientation of the magnetic moments, and internal exchange interactions, which try to keep the actively aligned structures[2]. As the structures transition from an ordered to a disordered paramagnetic structure at T_C and T_N, an order–disorder transition occurs. Many, but not all, paramagnetic compounds experience an ordering transition upon cooling, and the temperature dependence of magnetic susceptibility, χ provides evidence for whether or not this is likely to occur. Magnetic susceptibility is inversely proportional to temperature in paramagnetic material, according to the simple Curie law[2]:

$$\chi = \frac{C}{T} \tag{2.19}$$

where T is absolute temperature and C is a material-specific Curie constant ($C = \frac{N_A \mu^2}{3k}$), where N_A is Avogadro's number, μ is magnetic moment and k is Boltzmann constant. When there is no spontaneous interaction between nearby unpaired electrons, a Curie response occurs. They do tend to align in a magnetic field, but this alignment becomes more difficult as temperature rises, and χ drops, see equation 2.19. When there is some spontaneous interaction between nearby spins, which may turn into an ordered magnetic structure at low temperatures, the Curie–Weiss law frequently provides a better fit to the high-temperature behavior in the paramagnetic region. Curie–Weiss law is given as[2]:

$$\chi = \frac{C}{T - \theta} \tag{2.20}$$

where θ is the Weiss constant. Figure 2.10.1 depicts these two types of behavior by plotting χ^{-1} against T. The plot extrapolates to 0 K for paramagnetic compounds with no tendency to magnetic order. There is already some local alignment of spins in paramagnetic substances that exhibit a tendency to ferromagnetic order, and is higher than in the simple paramagnetic case.

Also, with a positive value of θ, χ becomes infinite (as χ^{-1}goes to zero), which roughly corresponds to the ferromagnetic Curie temperature, T_C, below which the sample is ferromagnetic.

The χ values in antiferromagnetic paramagnetic materials may be lower than in simple paramagnetic materials. The Curie–Weiss plot is displaced to lower temperatures as a result, and the extrapolated θ value is below 0 K. Antiferromagnetism develops below T_N and Curie–Weiss behavior is broken when such temperatures are attained. Figure 2.10.1 depicts the behavior of paramagnetic substances or ferro and antiferro-magnetic substances in the paramagnetic state above T_C and T_N; it is idealized, and deviations from ideality do occur in practice. Curie–Weiss behavior is absent below T_C and T_N. At low temperatures, ferromagnetic compounds have extremely high susceptibilities, which rapidly drop as the temperature approaches T_C. For antiferromagnetic materials, χ is very small in well-ordered structures at low temperatures, but increases with increasing temperature (unlike ferromagnets) as some thermally induced disorder is introduced into the antiferromagnetic state; χ passes through a maximum at T_N and then decreases at higher temperatures, following Curie–Weiss behavior.

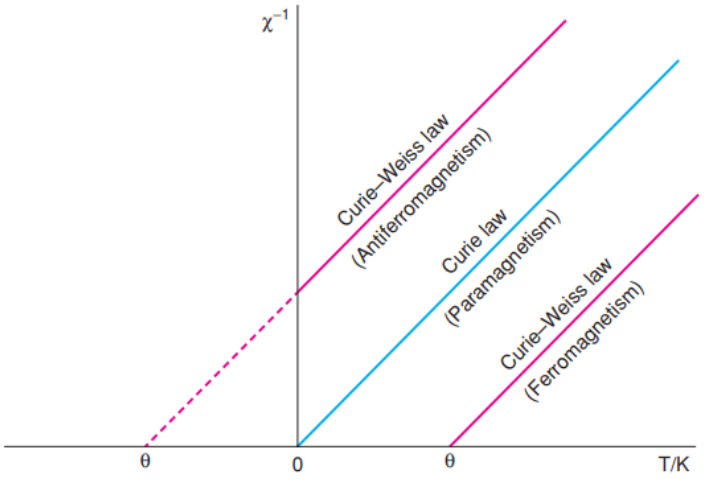

Figure 2.10.1: Reciprocal of susceptibility versus temperature for substances that are paramagnetic but may show magnetic ordering at low temperatures. Slope = C^{-1}. Image taken from[2].

2.11 Diamagnetism

All materials exhibit some diamagnetism, or a weak, negative magnetic susceptibility. A magnetic field induces a magnetic moment in a diamagnetic substance that opposes the applied magnetic field that created it. This effect is usually described from a classical perspective: the influence of a magnetic field on an electron's orbital motion results in a back electromagnetic field (back emf), which according to Lenz's law opposes the magnetic field that generated it. The Bohr–Van Leeuwen theorem[5][34], however, should cause us to be cautious of such framework is intended to illustrate how the application of a magnetic field to a classical system might produce a magnetic moment. Diamagnetism is a completely quantum mechanical phenomenon and should be treated as such.

2.12 Paramagnetism

The term paramagnetism refers to a positive susceptibility in which a magnetic field is used to induce a magnetization that aligns with the magnetic field that induced it. In the previous section we looked at materials that had no unpaired electrons and hence had no magnetic moment until a field was applied. We will focus on atoms having non-zero magnetic moments due to unpaired electrons. Because the magnetic moments on neighbouring atoms interact only very weakly with one another and can be presumed to be independent without an external magnetic field, these magnetic moments point in random directions. The degree of lining up (and thus the induced magnetization) depends on the strength of the applied magnetic field.
The total angular momentum J of an atom, which is the sum of the orbital angular momentum L and the spin angular momentum S, is associated with its magnetic moment[35].

[5]Bohr–Van Leeuwen theorem states that when statistical mechanics and classical mechanics are applied consistently, the thermal average of the magnetization is always zero.

2.13 Exchange interactions

The phenomena of long-range magnetic order is based on exchange interactions. When all you're dealing with is a bar magnet and a pile of iron filings, the exchange effect is weak and a little mysterious, because it seems unusual that you have to deal about exchange operators and identical particles[35]. But, as is often the case with magnetism, this is an example of how quantum mechanics is at the heart of a wide range of everyday phenomena. Charges of the same sign cost energy when they are close together and save energy when they are separated, hence exchange interactions are nothing more than electrostatic interactions.

For instance, for paramagnets the thermal energy of the interacting electrons is greater than the direct exchange interaction between electron spins. This means that after the external magnetic field is removed, the magnetization diminishes because the electron spins do not remain aligned. And for ferromagnets the magnetization is maintained even after switching off the external magnetic field because the exchange interaction is substantially bigger than the thermal energy. Only heating over the Curie temperature or more intense impacts cause the magnetization to disappear.

2.13.1 Direct exchange

Direct exchange occurs when electrons on neighboring magnetic atoms interact via an exchange interaction. This is due to the fact that the exchange interaction takes place without the use of an intermediary. Though this appears to be the most obvious path for the exchange interaction, in fact, physical situations are rarely so simple[35]. Because there is limited direct overlap between neighboring magnetic orbitals, direct exchange is usually inefficient in controlling magnetic characteristics. Rare earths, for example, have strongly localized $4f$ electrons that are very near to the nucleus, with low probability density extending beyond a tenth of the interatomic gap. This means that in rare earths, the direct exchange interaction is unlikely to be highly effective. Even in transition metals like Fe, Co, and Ni, where the $3d$ orbitals stretch further from the nucleus, it is hard to see how direct exchange could lead to the magnetic properties we

observe. Because these are metals, the role of the conduction electrons should not be ignored, and a proper description must account for both the localized and band character of the electrons. As a result, indirect exchange interactions must be considered in many magnetic materials.

2.13.2 Indirect exchange in ionic solids: superexchange

Magnetic ground states exist in a variety of ionic materials, including certain oxides and fluorides. MnO and MnF_2, for example, are both antiferromagnets, despite the fact that the electrons on Mn^{2+} ions in each combination have no direct overlap. Because the exchange interaction is generally fairly short-ranged, the longer-ranged interaction at work in this situation must be 'super'. The exchange mechanism at work here is known as superexchange. It is characterized as an indirect exchange connection between non-neighboring magnetic ions that is mediated by a non-magnetic ion that sits between them[35].

2.14 Ferromagnetism

Even in the absence of an applied field, a ferromagnet possesses a spontaneous magnetization. The magnetic moments all point in the same direction[6]. The appropriate Hamiltonian to solve for a ferromagnet in an applied magnetic field B is:

$$\hat{\mathcal{H}} = -\sum_{ij} \mathbf{J}_{ij}\mathbf{S}_i.\mathbf{S}_j + g_{\mu_B}\sum_j S_i.\mathbf{B} \tag{2.21}$$

To ensure ferromagnetic alignment, the exchange constants for nearest neighbors will be positive in this scenario. The term Heisenberg exchange energy is the first term on the right [35]. The Zeeman energy is the second phrase on the right. To keep things easy, let's assume we're working with a system with no orbital angular momentum, thus L = 0 and J = S. Even without any applied field, the internal molecular field can align the moments at low temperatures. It is worth noting that the alignment of these magnetic moments generates the internal molecular field that

[6]In many ferromagnetic samples this is not true throughout the sample because of domains. In each domain there is a uniform magnetization, but the magnetization of each domain points in a different direction from its neighbours.

causes the alignment in the first place. Magnetic order is self-sustaining at low temperatures. Thermal fluctuations weaken the magnetization as the temperature rises, and at a critical temperature, the order disappears. This model is known as the Weiss model of ferromagnetism (see Section 2.10.2).

2.15 Antiferromagnetism

If the exchange interaction is negative, the molecular field is orientated so that nearest neighbour magnetic moments are antiparallel to one another. This phenomenon is known as antiferromagnetism. This occurs frequently in systems that can be thought of as two interpenetrating sublattices, one with magnetic moments pointing up and the other with magnetic moments pointing down. Each magnetic moment's closest neighbors will then be totally on the opposite sublattice. Assuming the molecular field on one sublattice is proportional to the magnetization on the other, also suppose that no magnetic field is applied. Applying a magnetic field to an antiferromagnet below T_N (see Section 2.10 and 2.10.2) is more complex than applying a magnetic field to a ferromagnet below T_C (see Section 2.10 and 2.10.2) because the direction in which the magnetic field is applied is significant. Because any energy savings on one sublattice is cancelled by the energy cost on the other sublattice if the magnetization on the two sublattices is equal and opposite, there is no longer an energetic advantages for the moments to line up along the field.

2.16 Rietveld Refinement

The Rietveld refining method (named after the Dutch physicist Hugo Rietveld) has shown to be particularly useful in confirming structural features in powdered samples. Rietveld refinement[31] is a whole-pattern refinement in which the experimental powder XRD profile is compared to a computed profile, with refinement parameters adjusted [2]. Peak intensities are governed by lattice parameters as well as atomic coordinates. The peak shapes of the powder pattern are affected by various of factors, including sample size and shape, incident beam characteristics,

and the diffraction equipment utilized. It is a least squares technique, in which parameters are changed to minimize the weighted sum of squared residuals. The R-factors used to measure the quality of the experimental fit are listed below;

$$\text{Weighted profile R-factor}, R_{\text{wp}} = \left[\frac{\sum_i w_i(y_i(\text{obs}) - y_i(\text{calc}))^2}{\sum_i w_i(y_i(\text{obs}))^2} \right]^{\frac{1}{2}} \tag{2.22}$$

$$\text{Weighted sum of squared residuals}, \bar{\text{S}} = \sum_i w_i(y_i(\text{obs}) - y_i(\text{calc}))^2 \tag{2.23}$$

$$\text{Profile factor}, R_p = \frac{\sum |y_i(\text{obs}) - y_i(\text{calc})|}{\sum y_i(\text{obs})} \tag{2.24}$$

$$\text{Expected profile R-factor}, R_{\text{exp}} = \left[\frac{\text{N} - \text{P} + \text{C}}{\sum_i w_i(y_i(\text{obs}))^2} \right]^{\frac{1}{2}} \tag{2.25}$$

where $w_i = \frac{1}{y_i(\text{obs})}$ is the weight experimental observations, N is the number of experimental observations, P is the number of fitting parameters, C number of constraints[30].

Goodness of fit: is how well the refined computed pattern manifests the collected data. The goodness of fit (GoF) is given by the ratio of the residuals (which compares the weighted profile residual R_{wp} and the expected error R_{exp}). As the value of χ^2 gets smaller the fit gets better.

$$\text{Goodness of fit, GoF or } \chi^2 = \frac{R_{\text{wp}}}{R_{\text{exp}}} \tag{2.26}$$

Bragg R-factor: is based on the combined intensity of reflections, and consequently sensitive to fits at the reflections. The R-factor is the closest approximation in single crystal studies.

$$\text{Bragg R-factor}, \text{R}_\text{B} = \frac{\sum |\text{I}_\text{k}(\text{obs}) - \text{I}_\text{k}(\text{calc})|}{\sum I_k(obs)} \tag{2.27}$$

where $I_{k(obs)}$ and $I_{k(calc)}$ are observed and calculated integrated intensities.

2.17 Specific heat of solids

A material's heat capacity, C, is the proportionality constant between the heat it absorbs or loses and the temperature change that results. Despite the word "constant," however, this amount can change with temperature and pressure, particularly near phase transitions where entropy changes significantly. The lattice, electronic, and magnetic characteristics of a material can all be determined using heat capacity. Heat capacity (or specific heat) can be defined in two ways. Understanding the magnetic structure of a material and its behavior as temperature and magnetic field change is dependent on this information. The first is to keep a constant volume, C_v, and the second is to maintain a constant pressure, C_p; where C_p is usually larger than C_v[36]. Mathematically the specific heat capacity at a constant volume is given by;

$$C_v = \left(\frac{\partial E}{\partial T}\right)_v \tag{2.28}$$

where E is energy and T is temperature. In 1819 Dulong and Petit measured the same value of C_v as 6 cal/mol/deg for the many solids[37]. This observation made them to conclude that specific heat for all solids and gases was about 6 cal/mol/deg. This stayed true until the C_v of diamond was measured. After measuring the C_v of diamond the result was different from the previous findings. Later Boltzman came up with a classical explanation for why this could happen for C_v vs T. First he was able to explain the high temperature behaviour using classical theory (classical equipartition theorem). Taking the partial derivative of the total energy ($3RT$) where R is universal gas constant and this gives the C_v of $3R$ (also called the Dulong and Petit limit), refer to 2.17.1. The second question is why the specific heat actually drops to small values and approaching zero as temperature decreases, this was explained by Einstein. He applied quantum theory of radiation to solids for the first time (the energy of the oscillator quantized). He made the assumption that a 3-D solid containing one mole of atoms (N_A) can be represented by $3N_A$ identical uncoupled oscillators vibrating at the same angular frequency,

ω_E (called Einstein frequency). Thus the specific heat is given by[38];

$$C_v = 3R\left(\frac{\hbar\omega_E}{KT}\right)^2 \frac{e^{\frac{\hbar\omega_E}{KT}}}{\left(e^{\frac{\hbar\omega_E}{KT}} - 1\right)^2} \tag{2.29}$$

here $\hbar$ is Planck's constant, $\frac{h}{2\pi}$ and ω_E is angular frequency. Although this is not complete since it doesn't include the zero point motion expression, it was a significant finding.

What affects the heat capacity on the material level? The largest contribution to heat capacity is lattice vibration. As we keep heating up the material the lattice can contribute more and more in different direction. At very low temperature since there is not enough energy to

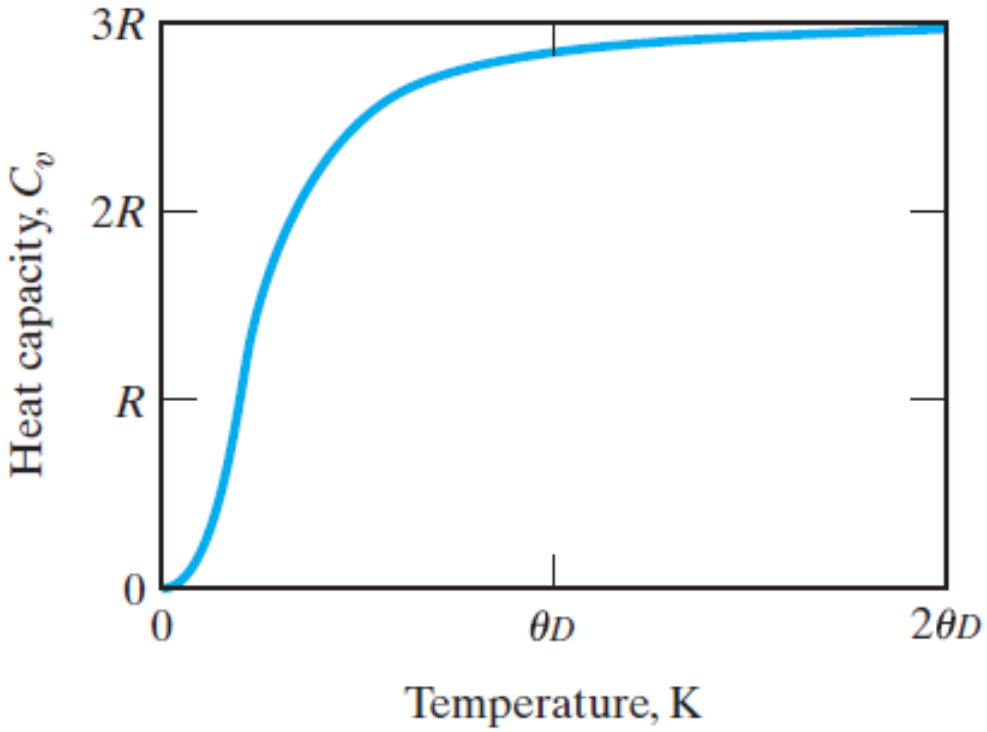

Figure 2.17.1: The temperature dependence of the heat capacity at constant volume, C_v. The magnitude of C_v rises sharply with a temperature near 0 K and above the Debye temperature (θ_D) levels off at a value of approximately 3 R. Image taken from[36].

excite the vibrations so the heat capacity goes to zero. At high temperature the vibration of all substances would be excited that is when it reaches a temperature called Debye[7] temperature. This is a temperature at which the heat capacity of all materials is constant.

2.17.1 Measuring specific heat of solids

The Quantum Design heat capacity option in the Physical Property Measurement System was used to measure specific heat capacity on the samples utilized in this study (PPMS). A weighed sample is cooled in vacuum to the lowest probing temperature required for heat capacity measurement[39]. The Quantum Design Heat Capacity option employs a relaxation technique that combines the highest measurement accuracy with reliable analysis methods. Relaxation approaches need precise time resolution of the sample platform's temperature response during the measurement cycle, as well as a precise correlation between the heater output and the temperature response[39]. The best signal-to-noise ratio requires quick, accurate thermometry. The data collecting element of a system is put to a lot of work because of these relaxation calorimetry requirements. Because relaxation times are generally short below 100 K, relaxation techniques have typically been applied at lower temperatures.

[7]The result shown in Figure 2.17.1 were created by Peter Joseph Wilhelm Debye (1884-1966), a Dutch-American physical chemist, as a modification of Einstein's theory of specific heats, including the then-newly developed quantum theory and the material's elastic constants. Debye made several contributions to physics and chemistry, including groundbreaking work on powdered material X-ray diffraction.

Chapter 3

Synchrotron X-ray and pair distribution function

The olivine structure allows for the formation of a sawtooth lattice by the atoms at 4*a* and 4*c*, and in the case of both Mn_2SiS_4 and Mn_2SiSe_4 by Mn. The central Mn—Mn bonds in the sawtooth are formed by the Mn at the 4*a* site (dark blue) and the Mn at the 4*c* site (light blue) near the tip of the triangles, as shown in Figure 3.0.1. The average bond distances and the angles of Mn_2SiS_4 and Mn_2SiSe_4 determined by Rietveld refinement of 11 BM data shown in Table 3.1. From the Mn-Mn distances, the sawtooth arrangement can be visualized as an isosceles triangle. This structural feature, with non-equivalent bond distances among the nearest-neighbors in the Mn-lattice, supports geometric frustration.

We investigated the crystal structures of Mn_2SiS_4 and Mn_2SiSe_4 at $T = 100$ K using high-resolution synchrotron X-rays collected at 11 BM. The X-ray diffraction patterns of both the compounds along with the refinements using Rietveld method are presented in Figure 3.0.2 (a) and (b), respectively. The olivine chalcogenides are prone to the development of impurity phases during the synthesis. As shown in Figure 3.0.2 only a low weight percentage of 4% MnS was detected in Mn_2SiSe_4. The refined lattice and atomic parameters of both Mn_2SiS_4 and Mn_2SiSe_4 at 100 K are collected in Table 3.1. The bond valence sum, BVS method[40] is used in this study to calculate the oxidation states of metal atoms.

$$V_i = \sum e^{\frac{R_0 - r_{ij}}{b}} \tag{3.1}$$

where V_i is the oxidation state of atom i, r_{ij} is the length of the bond between atoms i and j obtained experimentally, R_0 an empirical value of a determined cation-anion pair, and b is a universal parameter set to be equal to 0.37[41]. R_0 was obtained from the VESTA (Visualization for Electronic Structural Analysis) software package's bvparm2016.cif file[42].

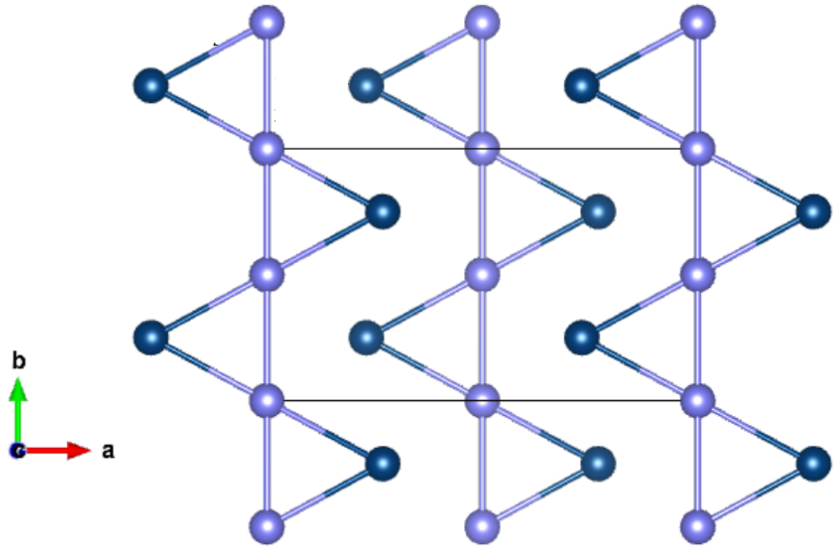

(a)

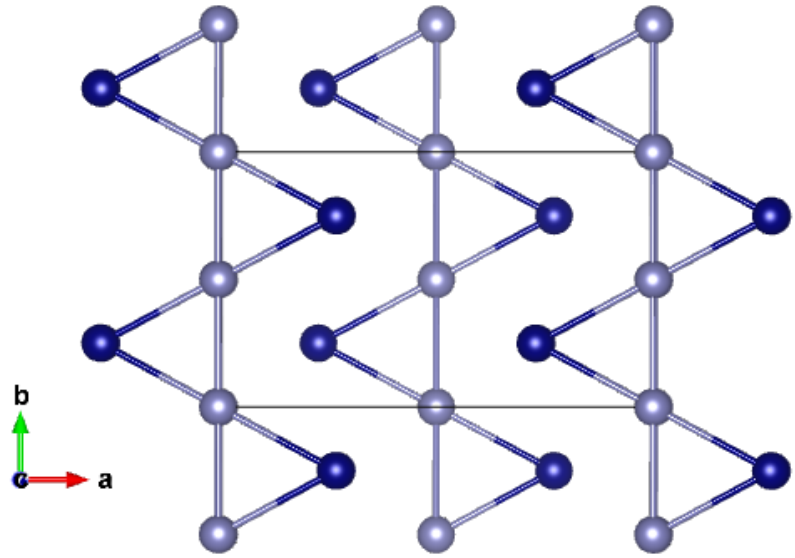

(b)

Figure 3.0.1: Sawtooth structure of (a) Mn_2SiSe_4 and (b) Mn_2SiS_4 synchrotron X-ray data obtained from 11 BM instrument.The Mn in this structure occupies two distinct Wyckoff positions, 4*a* (dark blue) and 4*c* (light blue). The Mn-Mn triangles form isosceles triangles.

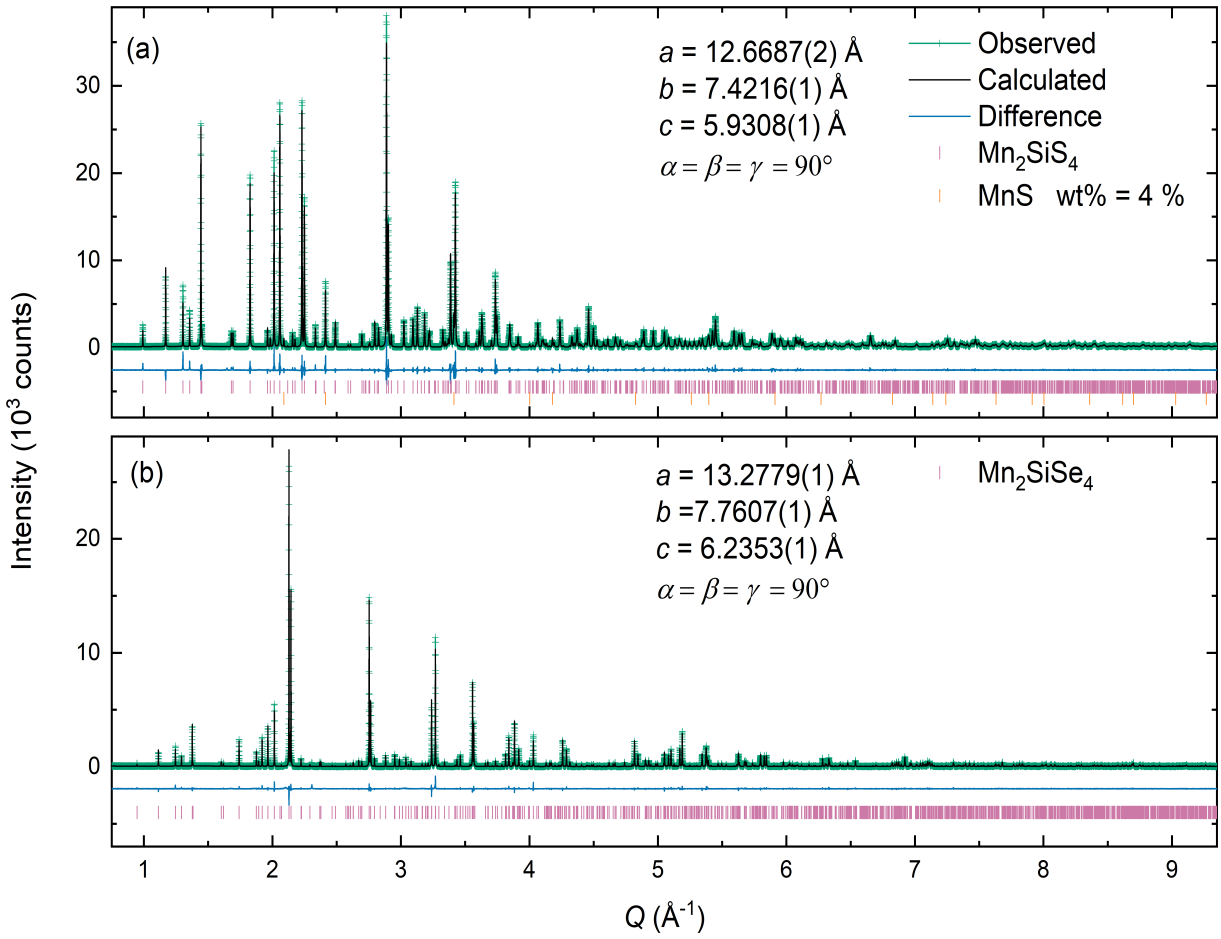

Figure 3.0.2: Synchrotron X-ray diffraction patterns along with Rietveld refinement fits for (a) Mn_2SiS_4 and (b) Mn_2SiSe_4, at $T = 100$ K. The data was collected at 11 BM, APS. The measured data points (green) and the coinciding solid line is the calculated pattern (black) using *Pnma* space group model. The horizontal(blue) curve at the bottom is the difference between the measured and the calculated patterns. Vertical bars mark the positions of nuclear Bragg reflections.

Table 3.1: The atomic parameters, bond distances and angles of Mn_2SiS_4 and Mn_2SiSe_4 at T = 100 K determined from Rietveld refinement of the synchrotron X-ray diffraction data from beamline 11 BM, APS. The refined lattice parameters of Mn_2SiS_4 are a (Å) = 12.6687(2), b (Å) = 7.4216(1), c (Å) = 5.9308(1); and a (Å) = 13.2779(1), b (Å) = 7.7607(1), c (Å) = 6.2353(1) for Mn_2SiSe_4 in Pnma space group. B_{iso} are the thermal parameters, "Occ." are the occupancies, and "Mult" are the multiplicities of the Wyckoff position. The best fit parameters are as follows: R_w = 9.20%, χ^2 = 2.1 for Mn_2SiS_4 and R_w = 11.13%, χ^2 = 1.3 for Mn_2SiSe_4.

Mn_2SiS_4	x/a	y/b	z/c	B_{iso}	Occ.	Mult
Mn1 (4a)	0.00000	0.00000	0.00000	0.0053(10)	0.500	4
Mn2 (4c)	0.22948	0.25000	0.51061	0.0054(11)	0.500	4
Si1 (4c)	0.41040	0.25000	0.09276	0.0032(16)	0.500	4
S1 (4c)	0.40639	0.25000	0.73822	0.0039(16)	0.500	4
S2 (4c)	0.56472	0.25000	0.23560	0.0045(18)	0.500	4
S3 (8d)	0.33300	0.02432	0.24609	0.0050(12)	1.000	8

Mn_2SiSe_4	x/a	y/b	z/c	B_{iso}	Occ.	Mult
Mn1 (4a)	0.00000	0.00000	0.00000	0.0023(2)	0.500	4
Mn2 (4c)	0.23104	0.25000	0.50931	0.0027(2)	0.500	4
Si (4c)	0.41093	0.25000	0.09450	0.0010(3)	0.500	4
Se1 (4c)	0.40717	0.25000	0.73532	0.0011(1)	0.500	4
Se2 (4c)	0.56860	0.25000	0.24182	0.0012(1)	0.500	4
Se3 (8d)	0.33167	0.02048	0.25101	0.0016(1)	1.000	8

Mn_2SiS_4	d_{Mn-S} (Å)	d_{Si-S} (Å)	d_{Mn-Mn} (Å)	∠Mn1-Mn2-Mn1 (°)	BVS
	2.5955(2)	2.1199(3)	3.7108(1)	56.8	4.0 (Si)
	2.6036(3)		3.8996(4)	61.6	2.2 (S)
					2.1 (Mn)
Mn_2SiSe_4	d_{Mn-Se} (Å)	d_{Si-Se} (Å)	d_{Mn-Mn} (Å)	∠Mn1-Mn2-Mn1 (°)	BVS
	2.7109(1)	2.2698(1)	3.8803(3)	56.9	3.8 (Si)
	2.7156(2)		4.0675(8)	61.5	2.1 (Se)
					2.0 (Mn)

3.1 Pair distribution function (PDF) analysis

Pair distribution function, PDF is the probability of finding an atom at a distance r from a given atom. Data collected at 11-ID-B (at APS) at 295 K with an energy of 58.6 keV ($\lambda = 0.2115$ Å) were subjected to atomic X-ray pair distribution function analysis. Fourier transform was used to get the reduced pair distribution function $G(r)$. As it is given in equation 3.3 $G(r)$ is the scattering vector, $S(Q)$ is the total structure function, where Q is the scattering vector, r is the interatomic distance in real space. The $G(r)$ in the scaling Q-range between $19.8 \leq Q \leq 23.8$ Å was obtained using GSAS-II. The structural information was extracted from the reduced PDF data using the PDFgui software program in the real-space range, $1.8 \leq r \leq 25$ Å.

$$G(r) = 4\pi r \rho_0 [g(r) - 1] \tag{3.2}$$

It measures the number of atoms in a unit-thickness spherical shell at r distance from a reference atom. When r approaches zero, it becomes a straight line through zero with a slope proportionate to the average number density, ρ_0 [43].

$$G(r) = \left(\frac{2}{\pi} \int_0^{Q_{max}} Q[S(Q) - 1] \sin(Qr)\, dQ \right) \tag{3.3}$$

where Q_{max} is the maximum value of Q up to which the diffraction experiment can be provided good data. The function $Q[S(Q) - 1] = F(Q)$ indicates the importance of the data at higher Q values. The data quality in the high Q region has a significant impact on the final result's quality. As we will deal with the total diffraction signals solely from the sample, we need to collect a background pattern from the sample container without the sample.

3.1.1 Data reduction

The first step in PDF data reduction is calibration of an area detector. By importing the *.tiff image from file menu item to read the data file into the opened GSAS-II project. The calibration we perform here will find the correct placement for the beam location (which defaults to the

image center) refer figure 3.1.1. The calibrant for 11- ID-B mail in program is cerium(IV) oxide, CeO_2 SRM674b as provided by National Institute of Standards and Technology, NIST. After the calibration, select points for using the left mouse button to click on at least five locations on the innermost ring. As each point is defined, a red "+" is added to the plot and hit right click to tell it is done.

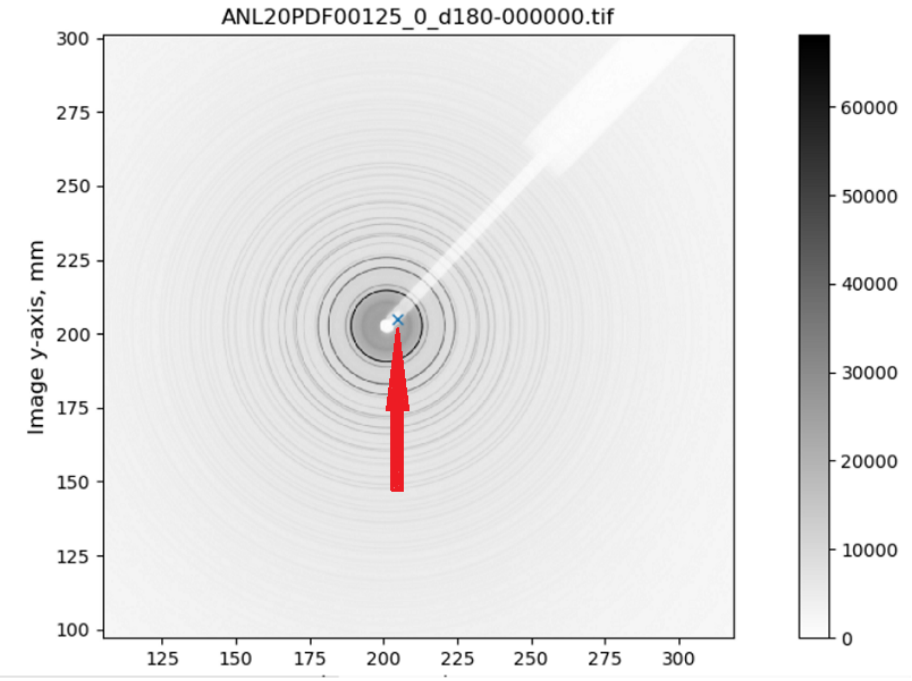

Figure 3.1.1: The 2D image before any calibration and data reduction is applied. In the inner ring in blue cross is where GSAS assumes the center of the detector.

3.1.2 Image controls

The calibration values needed to convert pixel locations to two-theta and azimuth are displayed in this window. Controls that determine how integration is done are also shown. This window's menu commands are used for calibration and integration (fitting the calibration values from a diffraction pattern image captured with a calibrant). After calibration, the integration of the area detector is set up. Change Bin style from 2θ to Q. Adjust the inner and outer 2θ values using the inner 2θ and outer 2θ controls. While adjusting the 2θ range, it's helpful to see the 2θ

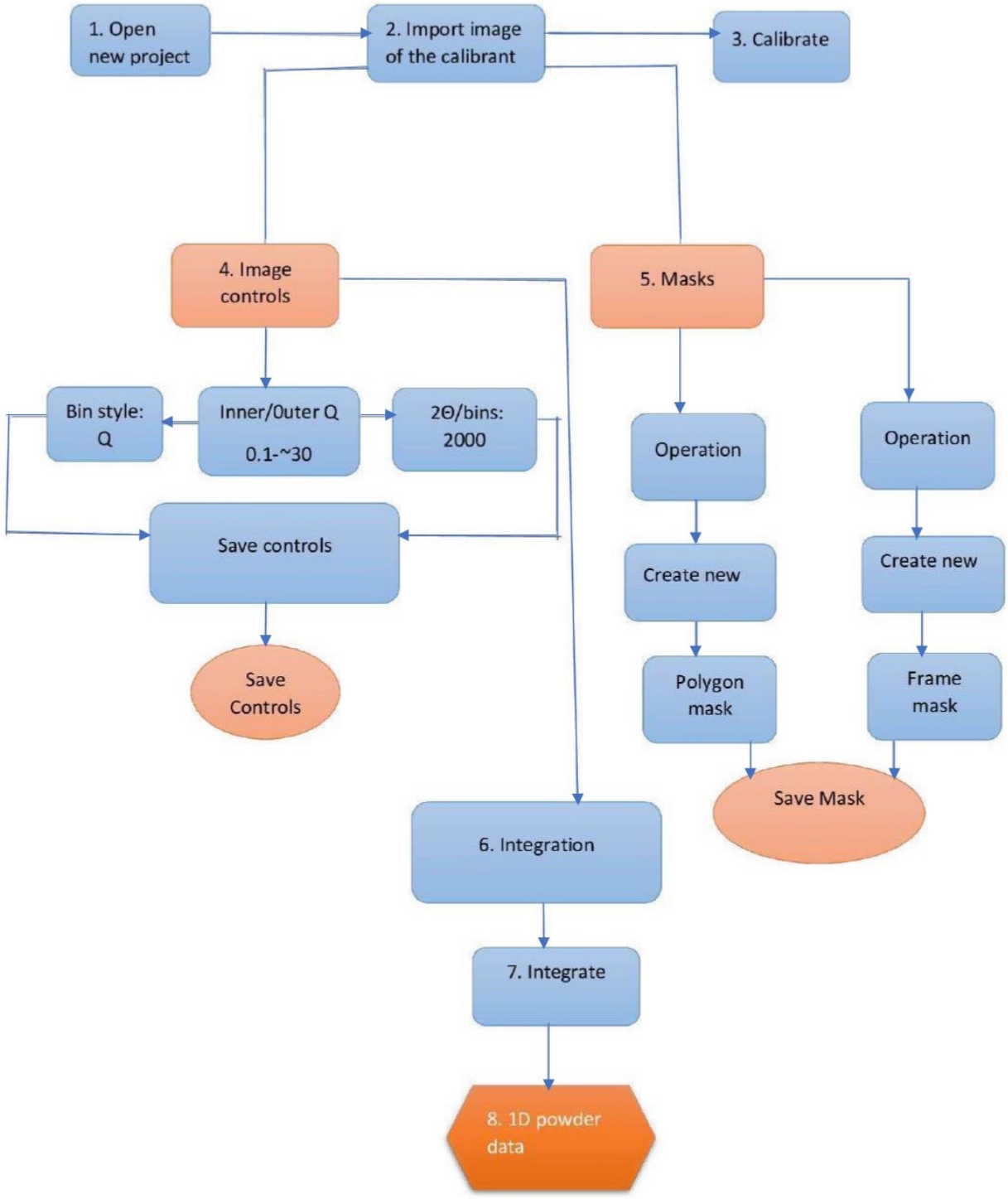

Figure 3.1.2: An outline of the flow of the data reduction with the different key steps required for successful X-ray powder data output. GSAS-II software was used for reduction.

boundaries on the plot visually, this is done using the "show integration limits" checkbox. By default, the inner limit is shown as a green ellipse at 2 degrees, while the outside limit is shown as a red ellipse at 5 degrees. These limitations can also be dragged to the required settings; the value is displayed in a small popup window. The values in the window can be saved to a file, read from a file, or copied to other pictures using other menu command, refer figure 3.1.2.

3.1.3 Masking

Image masks are used to mark parts of an image that should not be integrated, such as detector irregularities, beamstop shadows, single-crystal peaks from a mounting, and so on. A menu command or keyboard/mouse shortcuts can be used to create masks, refer figure 3.1.2. Although there are many different types of masks, these are the ones that are employed during data reduction.

Ring mask: obstructs a particular Bragg reflection (a ring placed relative to the image center). The location and thickness of the ring are specified in degrees 2-theta. Refer to image 3.1.3.
Polygon mask: occludes an arbitrary region formed by line segments connecting a sequence of points supplied in image coordinates (mm). The pixels inside the polygon mask are not used in the integration process. Refer to image 3.1.3.
Frame mask: obstructs an arbitary area formed by line segments connecting a series of points supplied in image coordinates (mm). A point is usually put near each corner of the image. For integration, only pixels inside the frame mask are used. There can only be one frame mask defined at a time. Refer to image 3.1.3. The raw data from 11-ID-B is not ready to use, it needs some correction such as background and masking the beam shadow.

3.1.4 PDF calculation

Next step in the PDF refinement process is to calculate the PDF. This is accomplished by first presenting a PDF calculation using GSAS-II, selecting a kapton background, and then selecting compounds with the appropriate ratio. Once we have a PDF, all we have to do now is optimize

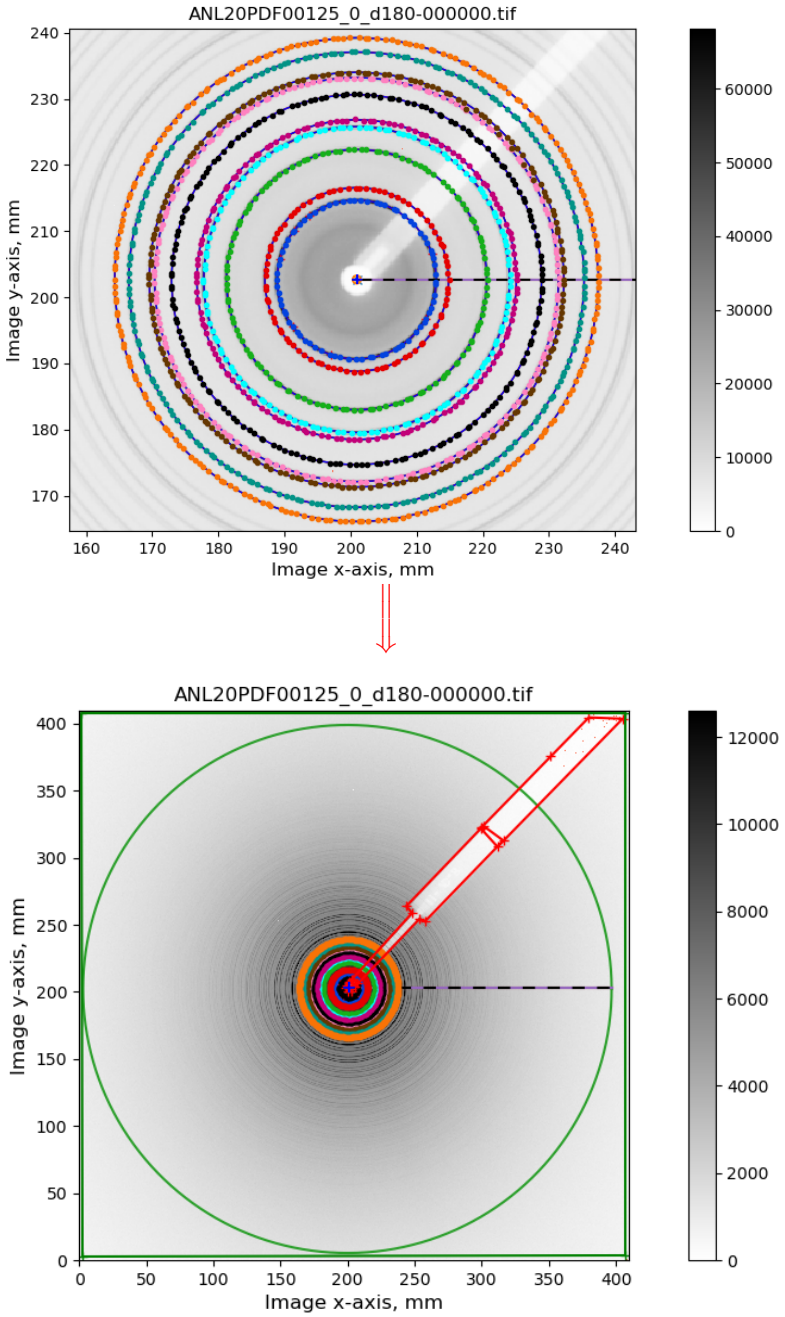

Figure 3.1.3: The image of the data taken before calibration (top panel). The first inner ring in blue is the center of the detector and the red ring the second from inside of top the image is the default where GSAS-II assumes the center detector to be. Masking of beam shadow (red rectangular bar) and frame mask (the outside green rectangle) for other artifacts (bottom panel). The big circle in green is the limit of integration. The red rectangular bar is the mask for the beam shadow.

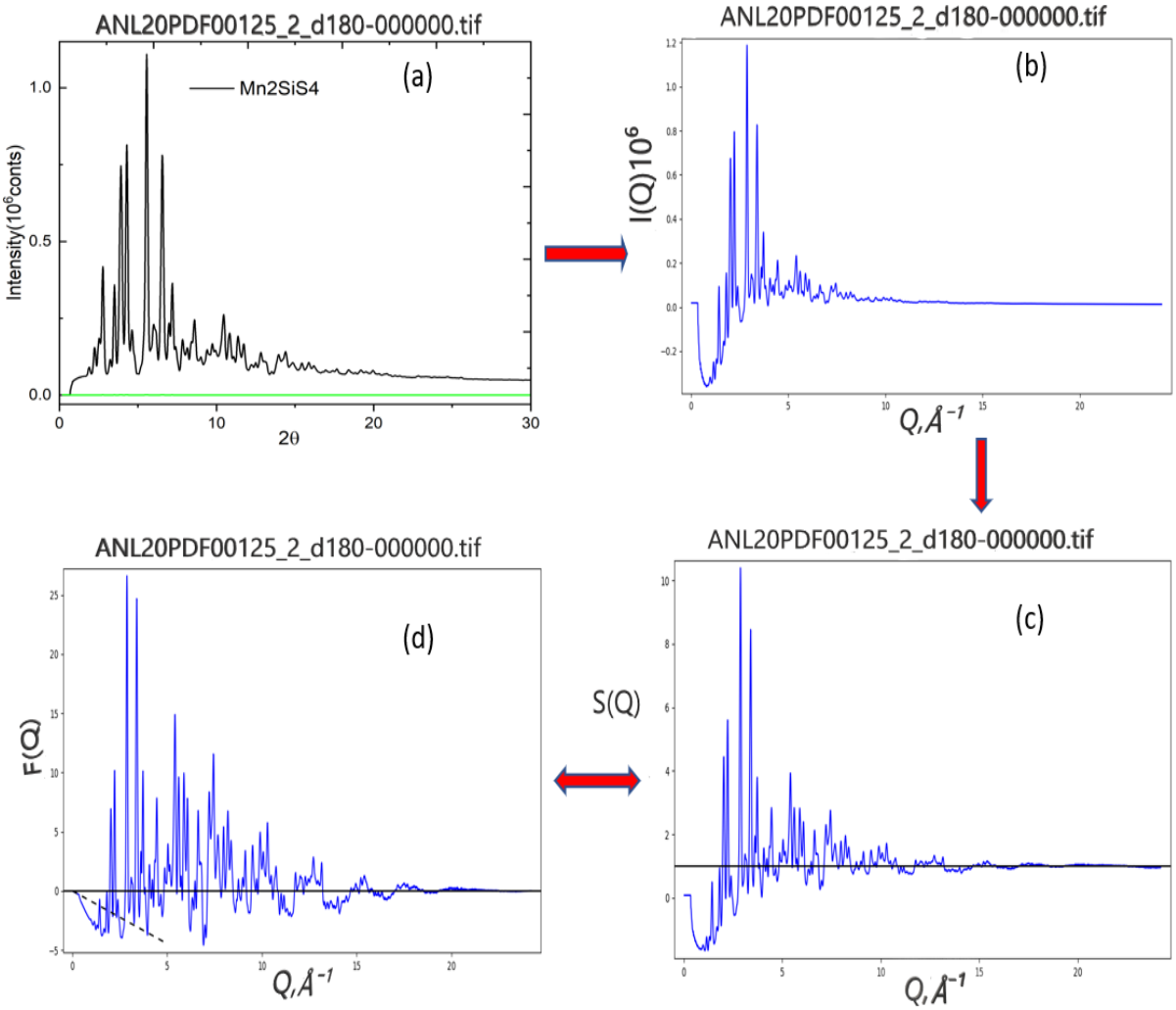

Figure 3.1.4: Schematic of the process for obtaining atomic pair distribution functions. (a) The powder diffraction data after the reduction from one dimensional image, (b) corrected X-ray intensity, $I(Q)$, (c) total scattering function $S(Q)$ and, (d) $F(Q)$.

it. By observing the progress, this can be repeated several times. The goal is to get the high Q region's deviation from zero for F(Q) and one for S(Q) to be as small as possible.

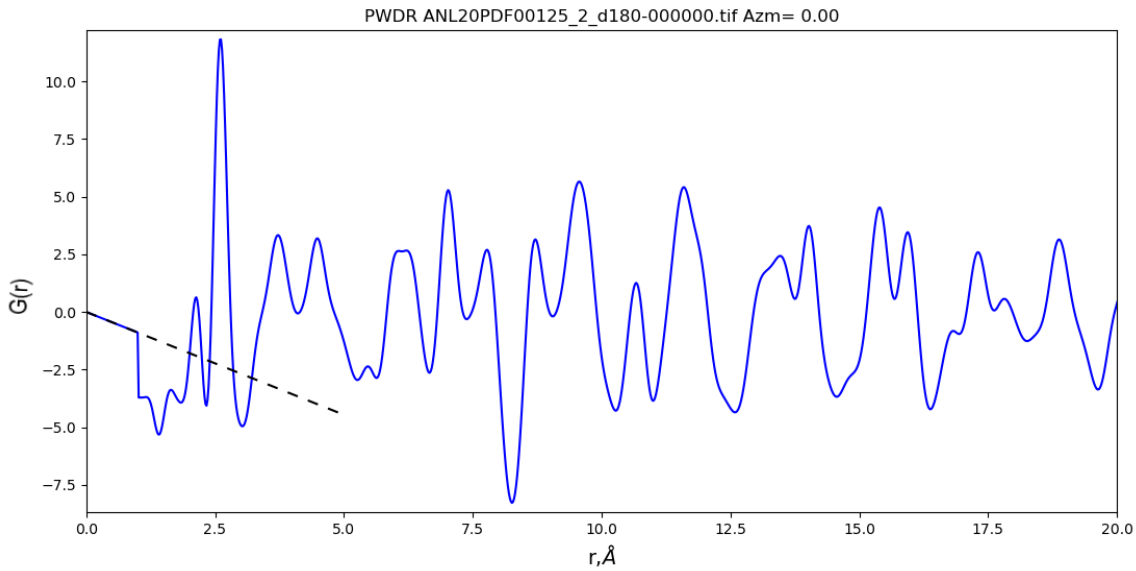

Figure 3.1.5: The PDF, *G(r)* as a function of r is obtained from F(Q) through a Fourier transform relationship shown in Section 3.1. The black dash line at low r is proportional to the average number density of the sample (should converge).

3.1.5 PDF peak fitting of $Mn_2Si\boldsymbol{X}_4$

The PDF refinements in Figure 3.1.6 (a, b) suggest that the local structure of Mn_2SiS_4 and Mn_2SiSe_4 are in agreement with the average structure deduced from high resolution X-ray diffraction. From the location of the initial peaks, the nearest-neighbor distances in the sawtooth lattice are estimated at 3.71Å for Mn_2SiS_4, and 3.88Å for Mn_2SiSe_4. The geometry of the peaks indicate that Mn triangles using pair distribution function analysis of the X-ray total scattering data, we find that the Mn triangles are nearly isosceles in both the olivine compounds. Thermal parameters of Mn_2SiS_4 and Mn_2SiSe_4 were determined from the analysis of G(r) shown in Figure 3.1.6 (a, b). All non-magnetic atoms were constrained to have isotropic thermal parameters while the magnetic atoms which constitute the sawtooth lattice (Mn1 and Mn2) were treated as anisotropic. The off-diagonal anisotropic terms were constrained $U_{12} = U_{13} =$

$U_{23} \equiv 0$.

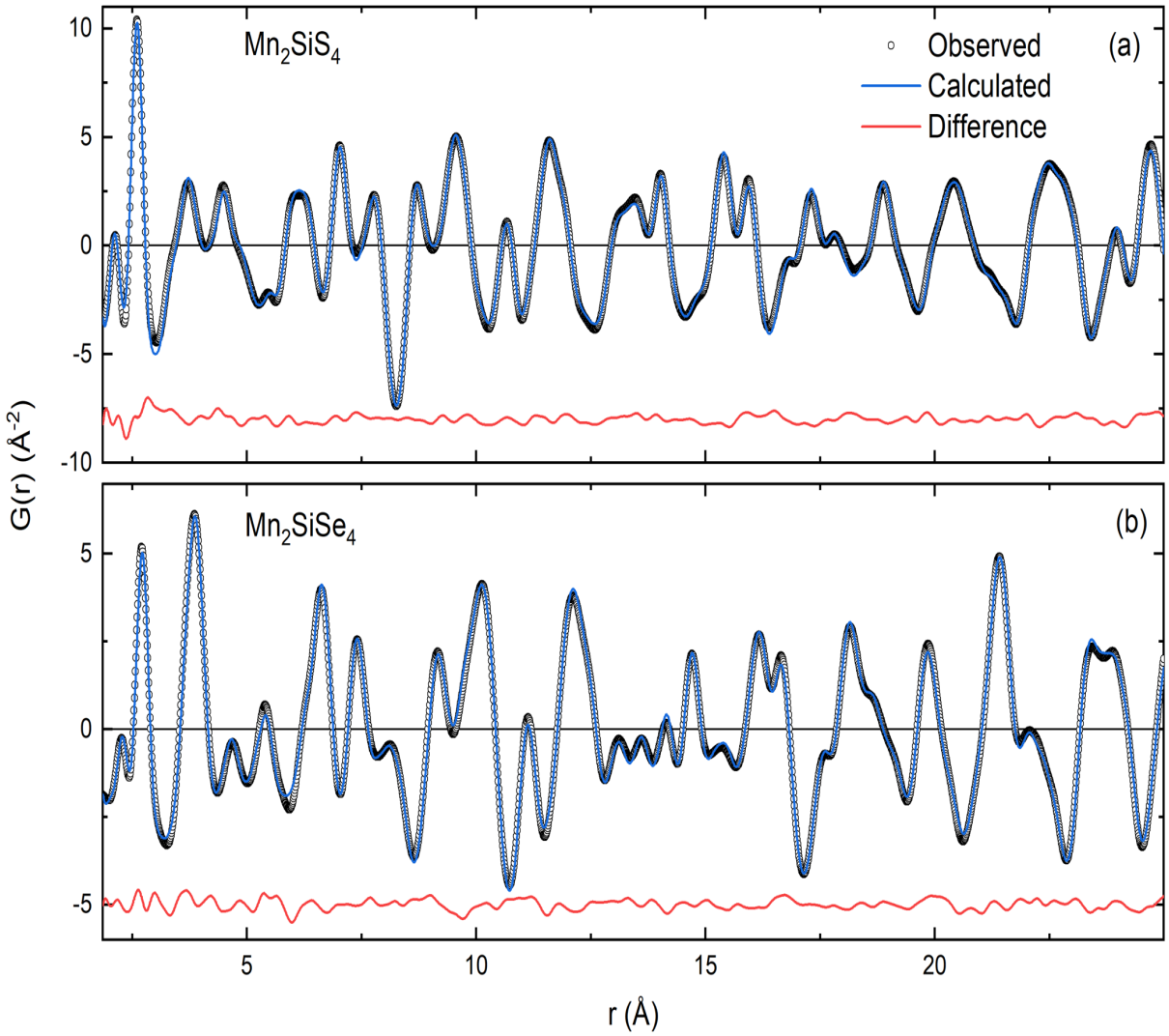

Figure 3.1.6: X-ray PDF refinement of (a) Mn_2SiS_4 and (b) Mn_2SiSe_4. The black open circle is the experimental data taken at 295 K, the solid cyan color the fit and the red is residual. PDFGUI[44] was used for refinement.

Table 3.2: The thermal parameters extracted from the X-ray pair distribution function analysis of Mn_2SiS_4 and Mn_2SiSe_4 at 295 K. The lattice parameters are $a = 12.7176(Å)$, $b = 7.4467(Å)$, $c = 5.94771(Å)$ for Mn_2SiS_4 and $a = 13.3286(Å)$, $b = 7.78358(Å)$, $c = 6.25402(Å)$ for Mn_2SiSe_4.

Mn_2SiS_4	U_{11}	U_{22}	U_{33}
Mn1	0.0165(3)	0.0202(3)	0.0150(3)
Mn2	0.0122(3)	0.0197(3)	0.0134(2)
Si1	0.0113(1)	0.0113(1)	0.0113(1)
S1	0.0125(2)	0.0125(2)	0.0125(2)
S2	0.0148(2)	0.0148(2)	0.0148(2)
S3	0.0109(7)	0.0109(7)	0.0109(7)
S4	0.0159(8)	0.0159(8)	0.0159(8)

Mn_2SiSe_4	U_{11}	U_{22}	U_{33}
Mn1	0.0247(1)	0.0472(2)	0.0140(1)
Mn2	0.0256(1)	0.0225(1)	0.0271(1)
Si1	0.0240(1)	0.0240(1)	0.0240(1)
Se1	0.0125(0)	0.0125(0)	0.0125(0)
Se2	0.0136(0)	0.0136(0)	0.0136(0)
Se3	0.0129(4)	0.0129(4)	0.0129(4)
Se4	0.0137(4)	0.0137(4)	0.0137(4)

We observed that the thermal parameters of Mn_2SiS_4 were such that, $U_{22} > U_{11} \approx U_{33}$ suggesting that there is a preferred thermal mode along the b-axis for both Mn1 and Mn2 atomic positions while the other two modes are maintained almost symmetrical. In contrast, Mn_2SiSe_4 displays symmetrical thermal contributions in the Mn2 atomic site for $U_{11} \approx U_{22} \approx U_{33}$ implying an isotropic behavior along the edges of the sawtooth. The backbone of the sawtooth chain presents a higher value along the b-axis with with no contribution loss along the a-axis but reduced motion along the c-axis. This may be caused by a strain driven by the frustrated spin triangular system. The best fit parameters found to be: $\chi^2 = 4.1$, $R_w = 7.9\%$ for Mn_2SiS_4 and $\chi^2 = 1.8$, $R_w = 6.6\%$ for Mn_2SiSe_4.

Chapter 4

Neutron powder diffraction

Time-of-flight neutron powder diffraction was performed on Mn_2SiS_4 and Mn_2SiSe_4 in POWGEN[45] at the Spalliation Neutron Source in Oak Ridge National Laboratory using two central wavelengths (1.5 Å and 2.66 Å). Diffraction experiments at 200 K, 100 K, 90 K, 80 K, 70 K, 60 K, 50 K, 30 K, 25 K, 15 K, 10 K, 8 K, 4 K, and 1.8 K were performed using a wavelength of $\lambda = 2.665$ Å. At 200 K and 1.8 K diffraction patterns were also collected using $\lambda = 1.5$ Å. The Rietveld refinements using FULLPROF suite program are shown in Figure 4.0.2 (a) and (b) and in Figure 4.0.3 (a) and (b). All the diffraction peaks were satisfactorily indexed in an orthorhombic unit cell (space group: *Pnma*) with lattice parameters: $a = 13.28516(12)$Å, $b = 7.76595(7)$Å, $c = 6.23747(6)$Å, $a = 12.67925(12)$Å, $b = 7.42881(9)$Å, $c = 5.93395(7)$Å and are in agreement with the literature [46, 47]. At high temperature (200 K) shown in Figure 4.0.2 (a) and 4.0.3 (a) there is no magnetic Bragg peak contribution for both compounds (Mn_2SiS_4 and Mn_2SiSe_4), all the peaks are from nuclear structure. However at low temperature (2 K), large increase in intensity of certain Bragg peaks at high d-spacing values is noticed.

The color map in figure on 4.0.1(a) and 4.0.1(b) denotes high-intensity areas where a nuclear or magnetic Bragg peaks have been found. Long-range magnetic ordering is observed in both Mn_2SiS_4 and Mn_2SiSe_4 with a d-spacing of ≈ 13 Å. This is clearly shown in Figure 4.0.1 (a) which illustrates the emerging magnetic ordering below 70 K in Mn_2SiSe_4 and Figure 4.0.1(b) below 90 K in Mn_2SiS_4. A small impurity of MnS was found in the Mn_2SiS_4 samples utilized for the neutron diffraction measurements. As a result, MnS was used as a second phase in the refining of the 200 K data and was quantified at 3% by weight. The magnetic structure of MnS was added to the refining as a third phase since MnS is magnetic at 200 K. The antiferromagnetic

structure of MnS has a propagation vector of k (0.5 0.5 0.5)[48]. The magnetic propagation vector of Mn_2SiS_4 at 2 K was determined using the k-search feature in FULLPROF suite as k (0 0 0)[49]. This yielded k (0 0 0) for both compounds below magnetic ordering temperatures. The indices of a few strong magnetic reflections are indicated in Figure 4.0.1 (a-b). The observed magnetic intensity indicate that the magnetic moments are normal to ab-plane in Mn_2SiSe_4 while the moments in Mn_2SiS_4 are nearly normal to ac-plane with possible component along b-axis. In Shubnikov notation, the Mn magnetic moments in this compound have 8 irreducible representations: $Pnma$, $Pn'm'a$, $Pnm'a'$, $Pn'ma'$, $Pn'm'a'$, $Pnma'$, $Pn'ma$, $Pnm'a$. P nm′a′, P n′ma′, P n′m′a′, P nma′, P n′ma and P nm′aRietveld refinements were performed to compare these space groups to the experimental diffraction data at 2 K. According to our findings, $Pnma$ has shown the best agreement. For Pnma with k (0 0 0), Mn at 4a Wyckoff position can have magnetic moment components along all the three crystallographic directions whereas, the moments of Mn at 4c are restricted along crystallographic b-axis. Rietveld refinements showed that the moment components of Mn along a and c axes are negligibly small (smaller than the error bars), so were constrained to be zero in the final refinements. The magnitudes of magnetic moments of Mn at both 4a and 4c sites are found to be nearly the same but opposite in sign and hence were constrained to be the same to obtain stable refinements. Up to the transition temperature T_N(S), the magnetic structure of Mn_2SiS_4 remains in $Pnma$. Figure 4.0.2 (c) shows the arrangement of Mn spins in the unit cell, while Figure 4.0.2 (d) illustrates the temperature-dependent change of the Mn magnetic moment. The data was subjected to a power-law fit, which is seen in the figure as a red line. As a result, the T_N was determined to be 83(2) K and this is in agreement with Ref[11]. The magnetic moment, m_{Mn}(T= 0), was calculated as $4.77(4)\mu_B$ using the power-law with exponent $\beta = 0.28(2)$.

The high-temperature structure of Mn_2SiSe_4 at 200 K was refined using only a nuclear-phase based on the $Pnma$ space group. Magnetic structure of Mn_2SiSe_4 was refined using the Pnma paramagnetic group in the same way as Mn_2SiS_4 with the propagation vector of k (0 0 0). As a result, Mn_2SiS_4 can have up to 8 irreducible representations, as shown above. The $Pnm'a'$

space group was found to be the best fit to the experimentally measured diffracted intensity. Figure 4.0.3 (c) shows a schematic diagram of the magnetic moment arrangement in the lattice, whereas Figure 4.0.3 (d) indicates the temperature-variation of the magnetic moment of Mn. m_{Mn} (T=0)= 4.38(5)μ_B and T_N(Se)=70.0(5) K are calculated from the refined magnetic moment values. We attempted to refine the magnetic moments of Mn(1) and Mn(2) independently since the Mn atom occupies two different Wyckoff positions in the lattice. However, there were no obvious differences.

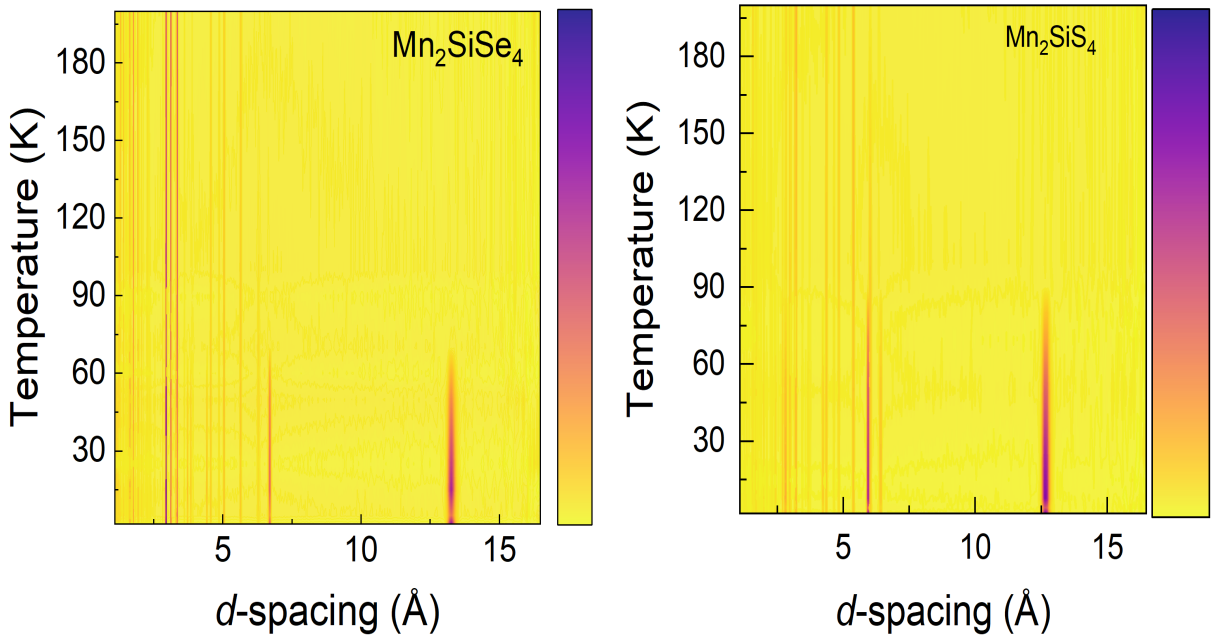

(a) (b)

Figure 4.0.1: The powder diffraction data of $Mn_2Si(S/Se)_4$ plotted as color maps in the temperature range 2-200 K displaying the emergence of magnetic Bragg peaks below 70 K for (a) Mn_2SiSe_4 and 90 K for (b) Mn_2SiS_4.

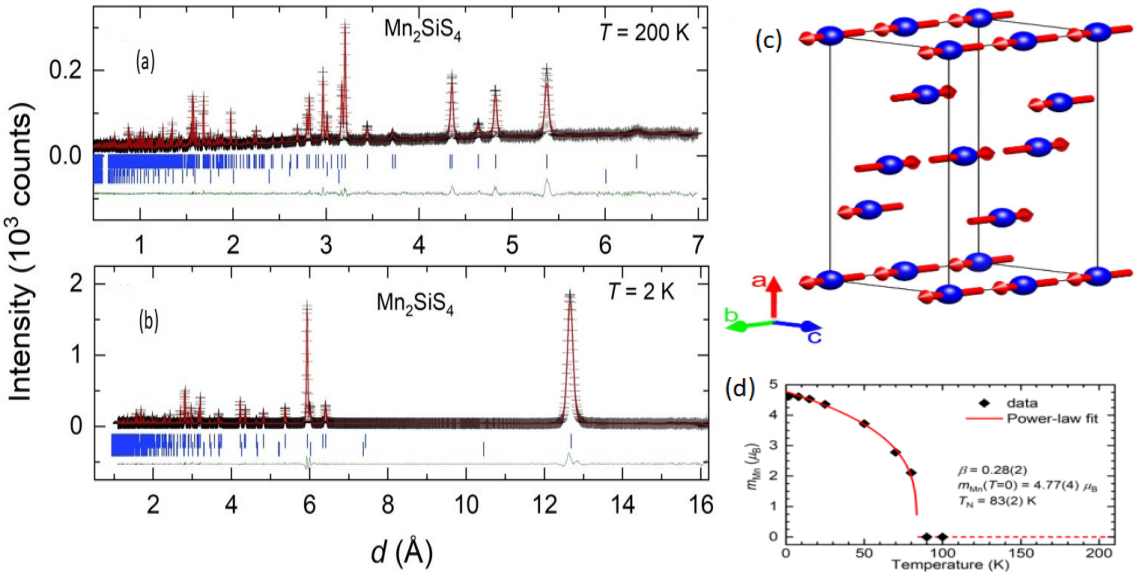

Figure 4.0.2: The Rietveld refined diffraction data of Mn_2SiS_4 at (a) 200 K > T_N(S) and (b) 2 K < T_N(S). The 2 K magnetic structure belongs to the magnetic space group *Pnma*. The magnetic structure of (c) Mn_2SiS_4. The temperature dependence of the magnetic moment of Mn (scatter), obtained from the refinement of neutron powder diffraction data for (d) Mn_2SiS_4.

Table 4.1: Refined atomic parameters of Mn_2SiS_4 at temperatures 200 K and 2 K.

T(K)	a (Å)	b (Å)	c (Å)	χ^2	R_p	R_{wp}	Major-phase	MnS
200	12.67925(16)	7.42881(9)	5.93395(7)	4.17	16.2	9.89	97.46(0.25)	2.54(0.03)
2	12.64918(19)	7.41355(12)	5.92708(8)	8.28	12.1	11.2	99.92(0.50)	0.08(0.0)

Table 4.2: Refined atomic parameters of Mn_2SiSe_4 at temperatures 200 K and 2 K.

T(K)	a (Å)	b (Å)	c (Å)	χ^2	R_p	R_{wp}	Major-phase	MnSe
200	13.28516(12)	7.76595 (7)	6.23747 (6)	5.79	11.1	7.42	98.35(0.23)	1.65(0.04)
2	13.25081(19)	7.74814(11)	6.22799(9)	48.9	13.9	14.6	100.00(0.38)	0.0

4.0.1 Inelastic neutron scattering of $Mn_2Si\boldsymbol{X}_4$

The magnetic excitations in Mn_2SiS_4 and Mn_2SiSe_4 were studied using inelastic neutron scattering on the thermal triple-axis spectrometer (TRIAX) at the University of Missouri Research

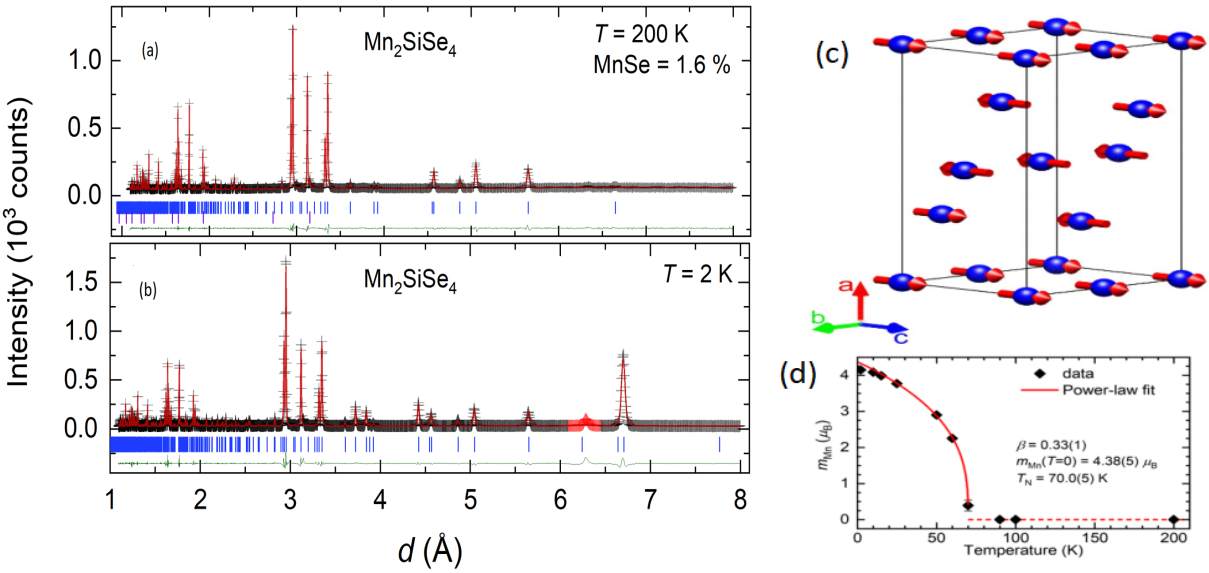

Figure 4.0.3: Similarly the refinement results of Mn_2SiSe_4 at 200 K are shown in (a) and 2 K in (b). The magnetic structure in this case is $Pnm'a'$. The magnetic structures of (c) Mn_2SiSe_4. The temperature dependence of the magnetic moment of Mn (scatter), obtained from the refinement of neutron powder diffraction data for (d) Mn_2SiSe_4.

Reactor (MURR). The raw data counts of the inelastic neutron data were corrected for the Bose thermal population factor. The resulting corrected intensity is plotted for T = 4.5 K well below the ordering temperature as Q-E maps in Figure 4.0.4(a) and (b) for Mn_2SiS_4 and Mn_2SiSe_4, respectively. Features consistent with extended spin-waves in a three-dimensional ordered anti-ferromagnet emanate from the ordering wave vector position Q = 1Å^{-1}. A band located at T $\sim$ 4.5 meV is observed to extend through the measured Q-range for both compounds. Figures 4.0.4(c) and (d) show the scattered inelastic intensity (thermal population corrected) well above the ordering temperature (T = 125 K). Correlations near the ordering wave vector position are seen to persist at these temperatures, particularly for Mn_2SiS_4. We attribute this signal to fluctuating super-spins associated with magnetic clusters formed above T_N. We note that this is consistent with the diffuse scattering observed in the neutron diffraction profile at the same temperature and with the observation of low heat capacity change across the magnetic ordering transition. We note that the somewhat higher coherent neutron scattering cross section of Se (σ = 7.98 barns) compared to that of S (σ = 1.02 barns) results in an increased contribution from phonons that appears as broad signal in the high-Q, high-E region of the colormap.

Figures 4.0.4 (e) and (f) draw out the main features observed in the inelastic spectra. Panel (e) depicts the measured intensity at the ordering wave vector (Q = 1Å^{-1}) for each of the two compounds and at both measurement temperatures. A peak at the band energy of 4.5 meV stands out prominently for Mn_2SiS_4, whereas more signal is shifted to lower energies for Mn_2SiSe_4 effectively washing out the weaker band feature. Taking a cut in the constant-E direction at this E = 4.5 meV value, however, shows the peak feature for Mn_2SiSe_4 as well as Mn_2SiS_4. The feature near Q = 1Å^{-1} , associated with short-range correlations, is evident in the line scan at 125 K, demonstrating the peak width of 0.7 Å^{-1}, indicating a correlation length for the spins of about 9 Å. This value agrees well with the interchain distance, which makes sense because we know that the intrachain ordering is FM, whereas the short-range correlations are associated with the AFM ordering wave vector suggesting that it originates from incipient coupling between sawtooth chain segments.

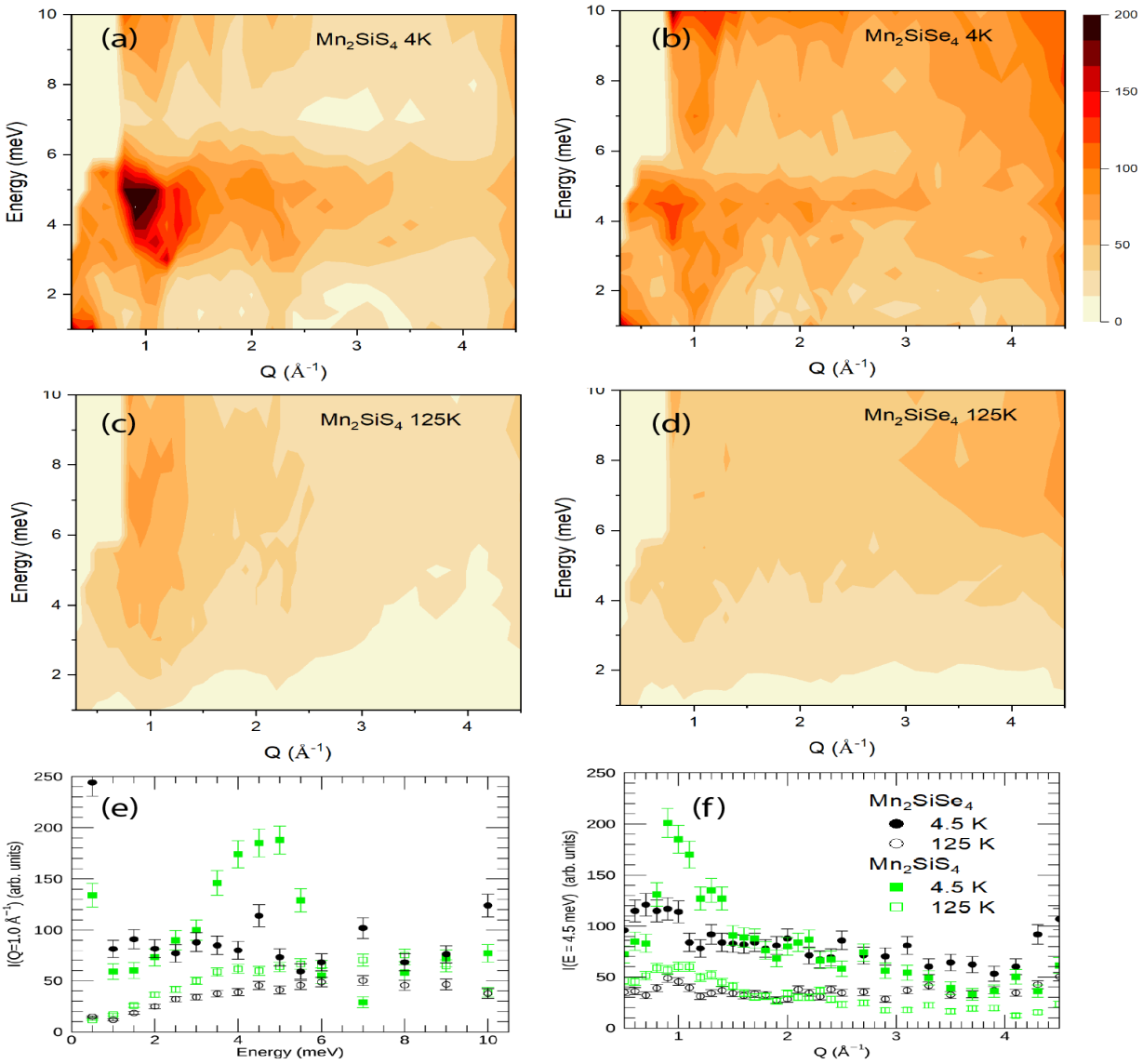

Figure 4.0.4: The Q-E map of Mn_2SiS_4 and Mn_2SiSe_4 obtained from inelastic neutron scattering experiment at T = 4.5 K [(a) and (b), respectively] and T = 125 K [(c) and (d), respectively]. The intensities in each are corrected by the thermal population factor. The spectra at low temperature are consistent with three-dimensional long-range order, while the above TN spectra show the presence of short-range correlations centered at the same ordering wave vector and more prominent for Mn_2SiS_4. The salient features of the four Q-E maps is illustrated by (e) constant-E and (f) constant -Q plots. Solid symbols are at base temperature and open symbols at 125 K; black symbols are Mn_2SiSe_4, green symbols are Mn_2SiS_4. The persistence of the Q = 1$Å^{-1}$ feature is evident in the constant-E plot.

Chapter 5

Bulk properties of Mn_2SiX_4

This chapter discusses the bulk properties of $Mn_2SiX_4 (X = Si, Se)$, which is how the measurement of magnetic susceptibility, and specific heat of solids was taken.

5.1 Magnetic susceptibility

Magnetization M is traditionally described as the sum of magnetic moments per sample volume, which is measured in $(\frac{Am^2}{m^3})$ = A/m, the same units as magnetic field H[50]. The partial derivative of M with respect to an applied field is described as magnetic susceptibility χ. For realistic field strengths, M is frequently linear with H (as in antiferromagnets and paramagnets), therefore susceptibility can be represented as $\chi = \frac{M}{H}$. Thus, χ is a dimensionless quantity since M and H have the same dimensions. A vibrating sample magnetometer (VSM) with a superconducting quantum interference device pick up coil (SQUID) is used to measure the magnetic susceptibility[51]. According to Lenz's law, the VSM vibrates the sample while maintaining a constant magnetic field, causing an emf in the SQUID that is proportional to the magnetization of the sample.

We have characterized the bulk properties and confirmed the phase transitions in the samples of the present study using magnetic susceptibility and specific heat. The magnetic susceptibility was measured in field cooled (FC) and zero field cooled (ZFC) protocols. Direct current magnetization measurements with an external field of 500 Oe were performed in a Magnetic Property Measurement System (MPMS) SQUID in the temperature range 2-300 K. The phase transitions in Mn_2SiS_4 and Mn_2SiSe_4 are first characterized using bulk measurements of magnetic suscep-

tibility and specific heat. The FC and ZFC dc magnetic susceptibility, χ_{dc}(T), of Mn_2SiS_4 and Mn_2SiSe_4 are shown in Figure 5.1.1.

In Mn_2SiS_4 a magnetic phase transition is seen in χ_{dc}(T) as a sharp peak at T_N (S) $\approx$ 83 K, Figure 5.1.1 (a). The phase transition in Mn_2SiSe_4, on the other hand, is identified as the point of bifurcation in χ_{dc}(T), at T_N (Se) $\approx$ 65 K. Below T_N(Se), the χ_{dc}(T) goes through a broad feature that breaks reversibility between the FC and ZFC curves. The inverse magnetic susceptibility was analyzed using Curie-Weiss law, $\chi(T) = \frac{C}{T-\theta_{cw}}$ and the Curie-Weiss temperature θ_{cw} and the T_N were used to determine the frustration constant, $f = \frac{|\theta_{cw}|}{T_N}$. This revealed reasonably high frustration for Mn_2SiSe_4 with f(Se) = 5.2, compared to Mn_2SiS_4 with f(S) = 2.7. These results agree well with our previous findings[3] and a similar compound [52]. Previous work on the magnetic structure of Mn_2SiS_4 showed that there was a narrow region of spontaneous magnetization between 83 K and 86 K, and below 83 K canted antiferromagnetism progressed towards collinear arrangement on the b-axis at 4.2 K[53]. The magnetic models that are predicted in the work by Ref[53], are $Pnma$ (4.2 K), $Pnma$ (80 K) and $Pn'm'a$ (83 K). Our results are in agreement with the space group model, however, proposes a ferromagnetic alignment of Mn spins. . The inverse magnetic susceptibility as a function of temperature and the plotted line using ideal Curie-Weiss law for Mn_2SiS_4 and Mn_2SiSe_4, are shown in the insets of Figure 5.1.1 (a) and (b). We do not see direct signatures of diffuse magnetism in our diffraction data. But the diminished ferromagnetic moment is an indication. A negative Curie-Weiss temperature is found in both the olivine compounds despite the ferromagnetic ground state below the respective T_Ns. This in turn is an indication of the strong short-range spin fluctuations that extend up to $2T_N$, as also verified by previous work[46]. Short-range spin fluctuations responsive to temperature and magnetic field are thus suspected to be present in both Mn_2SiS_4 and Mn_2SiSe_4.

Mn_2SiSe_4 reportedly orders antiferromagnetically below T_N (Se) $\approx$ 66 K while Mn_2SiS_4, below T_N (S) $\approx$ 83 K[3]. Mn_2SiSe_4 possesses a magnetic easy axis along the crystallographic c direction of the orthorhombic cell[46]. In this compound, the average magnetic structure

remains ferrimagnetic. Mn_2SiSe_4 displays pronounced field and temperature cycling dependencies in magnetic susceptibility[46] compared to the S-counterpart, and has a wider temperature range by the maximum seen in the magnetic susceptibility curve (between 66 K and 17 K, which is almost 50 K spread)[46, 54]. The broadness of the transition in magnetic susceptibility of Mn_2SiSe_4 and the hysteresis-like effects suggest a frustrated magnetic ground state.

5.2 Specific heat

The total specific heat of Mn_2SiS_4 and Mn_2SiSe_4 was analyzed by fitting the experimental data to a model consisting of lattice (C_p^{Einstein} and C_p^{Debye}) and electronic (C_p^{linear}) contributions such that, $C_p^{\text{total}}(T) = C_p^{\text{linear}} + C_p^{\text{Einstein}} + C_p^{\text{Debye}}$. The individual contributions mentioned above can be expressed as follows:

$$
\begin{aligned}
C_p^{\text{linear}} &= \gamma T, \\
C_p^{\text{Einstein}} &= 3rR \sum_i a_i \frac{x_i^2 e^{x_i}}{(e^{x_i}-1)^2}, \\
C_p^{\text{Debye}} &= \frac{9rR}{x_D^3} \int_0^{x_D} \frac{x_D^4 e^{x_D}}{(e^{x_D}-1)^2} dx_D.
\end{aligned}
$$

In the equations above, $x_D = \hbar\omega_D/k_BT$, $x_i = \hbar\omega_E/k_BT_i$, and r is the number of atoms, a_i are weight-factors of the different phonon modes, γ is the coefficient of linear-T contribution to specific heat whcih comes from electronic degrees of freedom. Mn_2SiS_4 has a γ value of 0.19(2) J/mol K^2 based on a temperature fit in the range of 2-250 K. The fit yielded θ_D(S) = 242(1)K and θ_E(S) = 626(3) K for Debye and Einstein temperatures, respectively. The $C_{p(T)}$ for Mn_2SiSe_4 was calculated using solely the lattice contribution, which included Einstein terms, and yielded θ_{E1}(Se) = 744(3) K and θ_{E2}(Se) = 128(2) K. $S_{mag} = \int_{T_1}^{T_1} (\frac{dC_{mag}}{T}) dT$, where T_1 = 60 K and T_2 = 110 K, was used to calculate the magnetic entropy of Mn_2SiS_4 displayed in the inset of Figure 5.2.1. At the phase transition temperature, T_N (S), the magnetic entropy was equal to 2 J/mol K. This is about 13.5% of total spin-only entropy (S = 5/2). Earlier studies, especially using specific heat analysis, have pointed out the very low entropy released at the phase transition

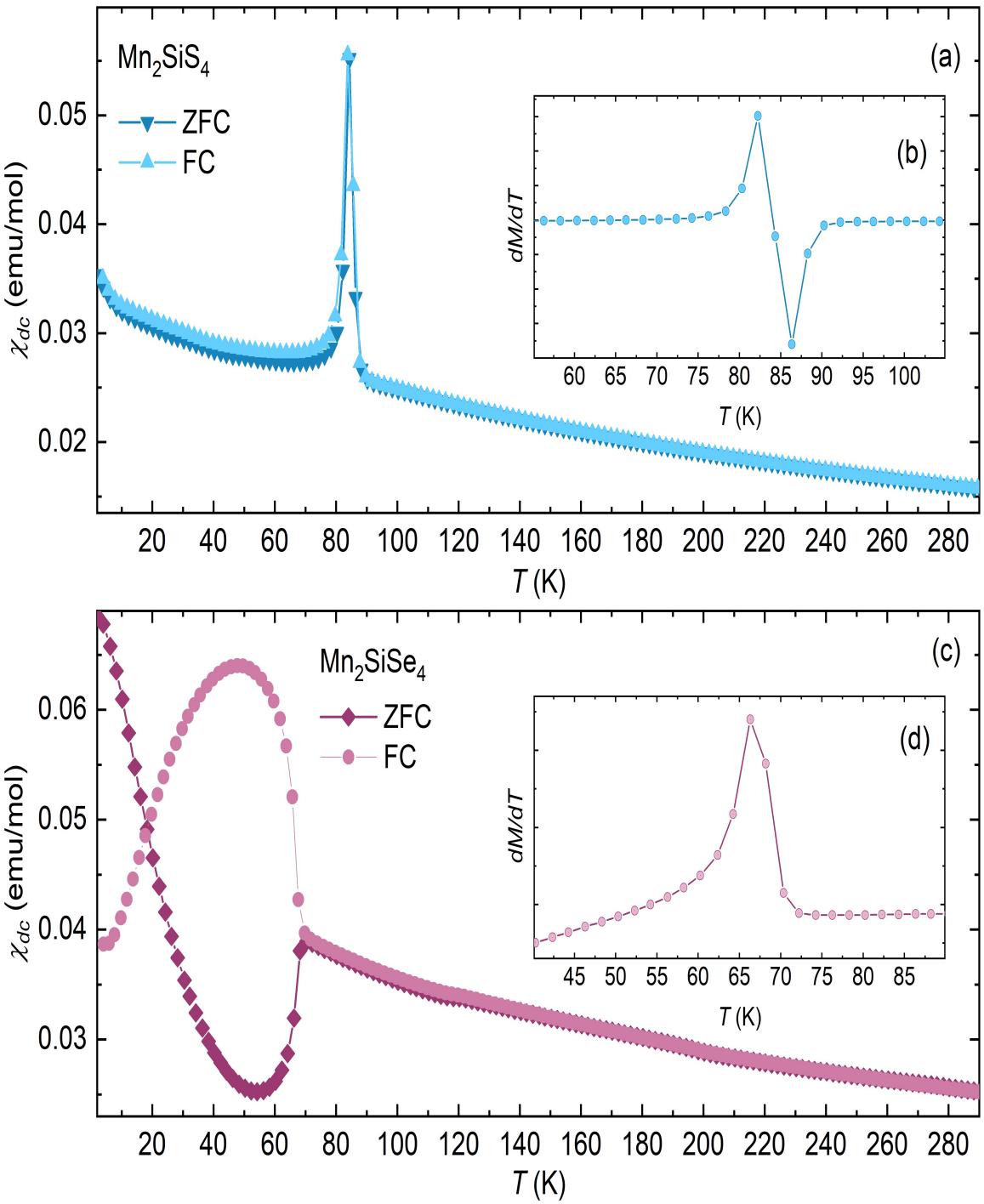

Figure 5.1.1: The dc magnetic susceptibility $\chi_{\rm dc}(T)$ of (a) Mn_2SiS_4 and (b) Mn_2SiSe_4. The insets of (a) and (b) show the derivative of magnetic susceptibility.

temperature of Mn_2SiS_4. For example, Ref [11] reports that only a release of 1.4% to 5% of Rln(6) is observed in the specific heat of Mn_2SiS_4. This was attributed to the fact that intensity of purely magnetic reflections were observed upto 140 K in neutron scattering experiments. These claims can be put to test if single crystals of Mn_2SiX_4 are synthesized. Alternatively, diffuse scattering experiments using polarized neutrons could help in the case of powder samples.

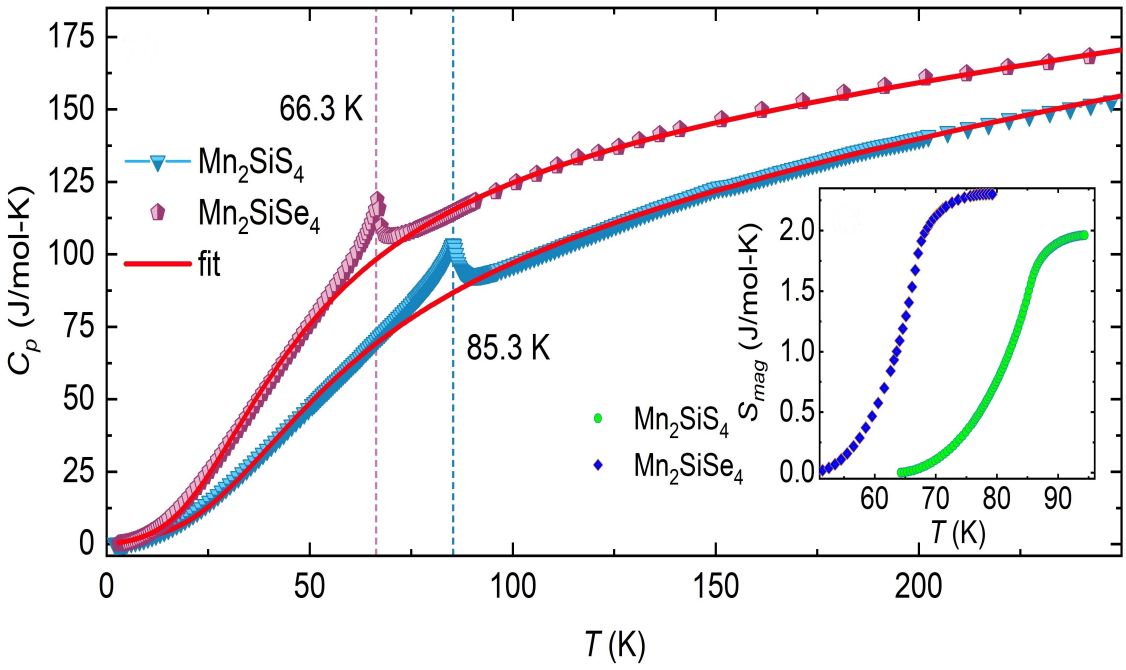

Figure 5.2.1: The specific heat C_p(T) of Mn_2SiS_4 and Mn_2SiSe_4 corroborates the phase transitions at T_N = 66.3 K and T_N = 85.3 K respectively. The solid lines overlapping on the data points are the curve fits that model the lattice specific heat incorporating a T-linear term, Debye and Einstein terms. The vertical dashed lines mark the location of the peak in specific heat. The inset shows the magnetic entropy of Mn_2SiS_4 (right green curve) and Mn_2SiSe_4 (left curve).

Chapter 6

Summary

In conclusion, we have presented the crystal and magnetic structures of the olivine chalcogenides, $Mn_2SiX_4 (X = S, Se)$, determined from X-ray and neutron diffraction data. The average and local crystal structure of the two title compounds, Mn_2SiS_4 and Mn_2SiSe_4 are investigated in detail using high-resolution X-ray synchrotron diffraction and the local structure through pair distribution function analysis of the X-ray total scattering data. Both Mn_2SiS_44 and Mn_2SiSe_4's Mn-triangles, which make up the sawtooth, are found to be isosceles triangles. The average magnetic structure determined through neutron diffraction reveals long-range antiferromagnetic order for both the compounds. Below the magnetic transition temperature, the magnetic structure of Mn_2SiS_4 belongs to $Pnma$ magnetic space group whereas that of Mn_2SiSe_4 is $Pnm'a'$. Through a power-law analysis of the temperature variation of magnetic moment, we determine the magnetic phase transition temperatures of Mn_2SiS_4 and Mn_2SiSe_4 as 83(2) K and 70.0(5) K. The magnon excitation spectrum of these two olivine chalcogenides are reported for the first time, thereby allowing to identify an excitation at approximately 4.5 meV at 4.5 K. Our results will be useful in future studies focusing on the magnon bands and electronic structure investigating magnonic or thermoelectric applications of this class of materials.

References

[1] A.-M. Lamarche, G. Lamarche, C. Church, J. Woolley, I. P. Swainson, and T. Holden, "Neutron diffraction study of magnetic phases in polycrystalline mn_2sis_4," *Journal of magnetism and magnetic materials*, vol. 137, no. 3, pp. 305–312, 1994.

[2] A. R. West, *Solid state chemistry and its applications*. John Wiley & Sons, 2014.

[3] H. Nhalil, R. Baral, B. Khamala, A. Cosio, S. Singamaneni, M. Fitta, D. Antonio, K. Gofryk, R. Zope, T. Baruah *et al.*, "Antiferromagnetism and the emergence of frustration in the sawtooth lattice chalcogenide olivines $Mn_2SiS_{4-x}Se_x$ (x = 0-4)," *Physical Review B*, vol. 99, no. 18, p. 184434, 2019.

[4] S. J. Fredrick and A. L. Prieto, "Solution synthesis and reactivity of colloidal Fe_2GeS_4: a potential candidate for earth abundant, nanostructured photovoltaics," *Journal of the American Chemical Society*, vol. 135, no. 49, pp. 18 256–18 259, 2013.

[5] V. K. Gudelli, V. Kanchana, and G. Vaitheeswaran, "Predicted thermoelectric properties of olivine-type Fe_2GeCh_4 (Ch= S, Se and Te)," *Journal of Physics: Condensed Matter*, vol. 28, no. 2, p. 025502, 2015.

[6] I. Hagemann, P. Khalifah, A. Ramirez, and R. Cava, "Geometric magnetic frustration in olivines," *Physical Review B*, vol. 62, no. 2, p. R771, 2000.

[7] M. Zhitomirsky and H. Tsunetsugu, "Exact low-temperature behavior of a kagomé antiferromagnet at high fields," *Physical Review B*, vol. 70, no. 10, p. 100403, 2004.

[8] E. J. Bergholtz and Z. Liu, "Topological flat band models and fractional chern insulators," *International Journal of Modern Physics B*, vol. 27, no. 24, p. 1330017, 2013.

[9] G. Lau, B. Ueland, R. S. d. Freitas, M. Dahlberg, P. Schiffer, and R. Cava, "Magnetic

characterization of the sawtooth-lattice olivines ZnL_2S_4 (L= Er, Tm, Yb)," *Physical Review B*, vol. 73, no. 1, p. 012413, 2006.

[10] D. Sen, B. S. Shastry, R. Walstedt, and R. Cava, "Quantum solitons in the sawtooth lattice," *Physical Review B*, vol. 53, no. 10, p. 6401, 1996.

[11] A. Junod, K.-Q. Wang, G. Triscone, and G. Lamarche, "Specific heat, magnetic properties and critical behaviour of Mn_2SiS_4 and Fe_2GeS_4," *Journal of magnetism and magnetic materials*, vol. 146, no. 1-2, pp. 21–29, 1995.

[12] C. Brinker, K. Keefer, D. Schaefer, and C. Ashley, "Sol-gel transition in simple silicates," *Journal of Non-Crystalline Solids*, vol. 48, no. 1, pp. 47–64, 1982.

[13] B. D. Cullity, *Elements of X-ray Diffraction*. Addison-Wesley Publishing, 1956.

[14] "The Nobel Prize in Physics 1906- nobelprize.org," https://www.nobelprize.org/prizes/physics/1906/thomson/biographical/, [Accessed 14-Oct-2022].

[15] "Lattice Structures in Crystalline Solids chem.libretexts.org," https://chem.libretexts.org/Courses/BethuneCookman_University/B-CU%3A_CH-141_General_Chemistry_1/Map%3A_Chemistry_-_Atoms_First_(OpenSTAX)/10%3A_Liquids_and_Solids/10.6%3A_Lattice_Structures_in_Crystalline_Solids, [Accessed 16-Oct-2022].

[16] C. V. Stan, C. M. Beavers, M. Kunz, and N. Tamura, "X-ray diffraction under extreme conditions at the advanced light source," *Quantum Beam Science*, vol. 2, no. 1, 2018. [Online]. Available: https://www.mdpi.com/2412-382X/2/1/4

[17] T. Heitmann and W. Montfrooij, "Practical neutron scattering at a steady state source," *Columbia: Mizzou Media*, 2012.

[18] A. Sharma and D. Hesterberg, "Synchrotron radiation-based spatial methods in environmental biogeochemistry," *Multidimensional Analytical Techniques in Environmental Research, eds. RMBO Duarte and AC Duarte (Elsevier, BV, 2020)*, pp. 231–265, 2020.

[19] B. H. Toby and M. R. Suchomel, "Mail-in synchrotron powder diffraction at the aps," 2011.

[20] "11-BM FAQ - 11bm.xray.aps.anl.gov," https://11bm.xray.aps.anl.gov/faq.html, [Accessed 15-Oct-2022].

[21] B. H. Toby, Y. Huang, D. Dohan, D. Carroll, X. Jiao, L. Ribaud, J. A. Doebbler, M. R. Suchomel, J. Wang, C. Preissner *et al.*, "Management of metadata and automation for mail-in measurements with the aps 11-bm high-throughput, high-resolution synchrotron powder diffractometer," *Journal of Applied Crystallography*, vol. 42, no. 6, pp. 990–993, 2009.

[22] Aram, "synchrotron-around-the-world, slri.or.th," https://www.slri.or.th/en/index.php/synchrotron-around-the-world.html, [Accessed 19-Oct-2022].

[23] M. W. Terban and S. J. Billinge, "Structural analysis of molecular materials using the pair distribution function," *Chemical Reviews*, 2021.

[24] "Box, anl.app.box.com," https://anl.app.box.com/s/l3lgklgbaeoxgn1v3h52acb4nn7m4gvt/file/864966364432, [Accessed 16-Oct-2022].

[25] "A History of Neutron Scattering at ORNL Shull Wollan Center swc.ornl.gov," https://swc.ornl.gov/article/history-neutron-scattering-ornl, [Accessed 03-Nov-2022].

[26] C. G. Shull, "Early development of neutron scattering," *Rev. Mod. Phys.*, vol. 67, pp. 753–757, Oct 1995. [Online]. Available: https://link.aps.org/doi/10.1103/RevModPhys.67.753

[27] "Brockhouse and shull win the nobel prize in physics," *Neutron News*, vol. 6, no. 1, pp. 2–4, 1995. [Online]. Available: https://doi.org/10.1080/10448639508217669

[28] "Powder Diffractometer Neutron Science at ORNL neutrons.ornl.gov," https://neutrons.ornl.gov/powgen, [Accessed 01-Nov-2022].

[29] IAEA., *Measurement of residual stress in materials using neutrons.* International Atomic Energy Agency, 2005.

[30] E. H. Kisi and C. J. Howard, *Applications of neutron powder diffraction*. Oxford University Press, 2012, vol. 15.

[31] L. Lutterotti, "Introduction to diffraction and the rietveld method," *Laboratorio Scienza e Tecnologia dei Materiali*, pp. 6–20, 2006.

[32] J. Rodriguez-Carvajal, "Fullprof: a program for rietveld refinement and pattern matching analysis," in *satellite meeting on powder diffraction of the XV congress of the IUCr*, vol. 127. Toulouse, France:[sn], 1990.

[33] J. M. Coey, *Magnetism and magnetic materials*. Cambridge university press, 2010.

[34] "Wikiwand-wikiwand.com,-https://www.wikiwand.com/en/bohr%e2%80%93van_leeuwen_theorem," [Accessed 06-Nov-2022].

[35] S. Blundell, "Magnetism in condensed matter," 2003.

[36] J. F. Shackelford, *Introduction to materials science for engineers*. Pearson Upper Saddle River, 2016.

[37] T. H. Bindel and J. C. Fochi, "Guided discovery: Law of specific heats," *Journal of chemical education*, vol. 74, no. 8, p. 955, 1997.

[38] "Specific Heats of Solids farside.ph.utexas.edu," https://farside.ph.utexas.edu/teaching/sm1/Thermalhtml/node86.html, [Accessed 12-Oct-2022].

[39] H. C. O. U. Manual, "Physical property measurement system."

[40] T. Nguyen, "Bond valence sum: A powerful tool for determination of oxidation states of metal ions in coordination compounds," 2020.

[41] I. Brown, "Chemical and steric constraints in inorganic solids," *Acta Crystallographica Section B: Structural Science*, vol. 48, no. 5, pp. 553–572, 1992.

[42] K. Momma and F. Izumi, "Vesta: a three-dimensional visualization system for electronic and structural analysis," *Journal of Applied crystallography*, vol. 41, no. 3, pp. 653–658, 2008.

[43] S. K. Sinha, M. K. Sanyal, and C. K. Loong, *Advanced Characterization of Nanostructured Materials: Probing the Structure and Dynamics with Synchrotron X-rays and Neutrons*. World Scientific, 2021, vol. 21.

[44] "PDFgui DiffPy documentation." [Online]. Available: https://www.diffpy.org/products/pdfgui.html

[45] A. Huq, M. Kirkham, P. F. Peterson, J. P. Hodges, P. S. Whitfield, K. Page, T. Hűgle, E. B. Iverson, A. Parizzi, and G. Rennich, "Powgen: rebuild of a third-generation powder diffractometer at the spallation neutron source," *Journal of Applied Crystallography*, vol. 52, no. 5, pp. 1189–1201, 2019.

[46] F. Bodenan, V. Cajipe, G. Ouvrard, and G. André, "Low-temperature magnetic structure of the olivine Mn_2SiSe_4," *Journal of magnetism and magnetic materials*, vol. 164, no. 1-2, pp. 233–240, 1996.

[47] J. Fuhrmann and J. Pickardt, "Structure of Mn_2SiS_4," *Acta Crystallographica Section C: Crystal Structure Communications*, vol. 45, no. 11, pp. 1808–1809, 1989.

[48] M. VH *et al.*, "Magnetic structures of α-mns and mnse from 57 fe mossbauer spectroscopy," 1983.

[49] J.-H. Chung, K. Ohgushi, and Y. Ueda, "Magnetic phase diagrams of the multicritical olivine Mn_2SiS_4 and Mn_2GeS_4," *Journal of magnetism and magnetic materials*, vol. 322, no. 7, pp. 832–837, 2010.

[50] Wikipedia contributors, "Magnetic susceptibility Wikipedia, the free encyclopedia," 2022, [Online; accessed 11-October-2022]. [Online]. Available: https://en.wikipedia.org/w/index.php?title=Magnetic_susceptibility&oldid=1092378514

[51] A. Adeyeye and G. Shimon, "Growth and characterization of magnetic thin film and nanostructures," in *Handbook of Surface Science*. Elsevier, 2015, vol. 5, pp. 1–41.

[52] M. Solzi, C. Pernechele, G. Attolini, G. Delgado, and V. Sagredo, "Magnetic ordering of Mn_2GeS_4 single crystals with olivine structure," *Journal of Magnetism and Magnetic Materials*, vol. 498, p. 166164, 2020.

[53] A.-M. Lamarche, G. Lamarche, C. Church, J. Woolley, I. Swainson, and T. Holden, "Neutron diffraction study of magnetic phases in polycrystalline mn_2sis_4," *Journal of Magnetism and Magnetic Materials*, vol. 137, no. 3, pp. 305–312, 1994. [Online]. Available: https://www.sciencedirect.com/science/article/pii/0304885394907161

[54] S. Jobic, F. Bode, P. Le Boterf, G. Ouvrard *et al.*, "Structure refinement and magnetic behaviour of the only selenide in the olivine group family: Mn_2SiSe_4," *Journal of alloys and compounds*, vol. 230, no. 1, pp. 16–22, 1995.

Vita

I, Melaku Tafere was born and raised in Ethiopia and received my bachelor of physics from Wolaita Sodo University, Ethiopia. In 2016 I got a scholarship in the National Astrophysics and Space Science, NASSP at Cape Town University, South Africa. I completed my study and received MSc in Astrophysics and Space Science in 2019. In 2021 I got Msc and teaching assistant ship at the University of Texas El Paso, UTEP (Jan - Aug 2021, Jan - Dec. 2022).

During my stay at UTEP I gained the following experience; analysing powder X-Ray diffraction, pair distribution function and writing a proposal to national labs to get data (such as 11-BM and 11-IDB mail in programs), synthesising solid material, crystal growth and handling of hazardous materials. I have attended Texas Academy of Science (TAS) annual Conference held at University of Houston Clear Lake February 25-27 2022 and a poster presentation at UTEP.

Melaku S. Tafere

mstafere@miners.utep.edu